Energy Landscapes for Electronic Structure

Hugh G. A. Burton[1, 2, a)] and David J. Wales[2, b)]
[1)]*Physical and Theoretical Chemistry Laboratory, University of Oxford, South Parks Road, Oxford, OX1 3QZ, U.K.*
[2)]*Department of Chemistry, University of Cambridge, Lensfield Road, Cambridge, CB2 1EW, U.K.*

(Dated: 25 November 2020)

Orbital-optimised multiple self-consistent-field (SCF) solutions are increasingly being interpreted as mean-field approximations of diabatic or excited electronic states. However, surprisingly little is known about the topology of the electronic energy landscape from which these multiple solutions emerge. In this contribution, we extend energy landscape methods, developed for investigating molecular potential energy surfaces, to investigate and understand the structure of the electronic SCF energy surface. Using analytic gradients and Hessians, we systematically identify every real SCF minimum for the prototypical H_4 molecule with the 3-21G basis set, and the index-1 saddles that connect these minima. The resulting SCF energy landscape has a double-funnel structure, with no high-energy local minima. The effect of molecular symmetry on the pathways is analysed, and we demonstrate how the SCF energy landscape changes with the basis set, SCF potential, molecular structure, and spin state. These results provide guiding principles for the future development of algorithms to systematically identify multiple SCF solutions from an orbital optimisation perspective.

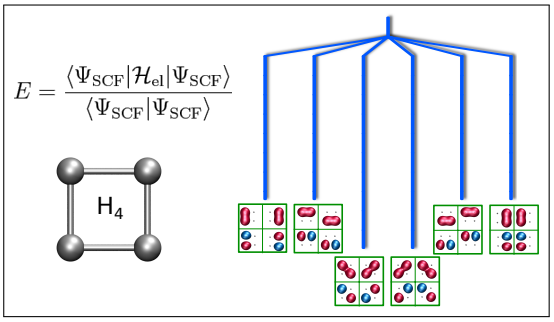

I. INTRODUCTION

There is never a unique self-consistent-field (SCF) solution for a molecule. Every physical system must always have at least two solutions: the global minimum and maximum of the SCF energy. Most cases will also exhibit additional solutions corresponding to local minima, maxima, or saddle points. These multiple SCF solutions have long been a source of fascination due to their inherent links with symmetry-breaking,[1–4] static electron correlation, and the breakdown of single-reference wave function approximations.[5–7] More recently, higher-energy solutions have been proposed as mean-field approximations to excited states,[8–13] while symmetry-broken solutions are often interpreted as quasidiabatic configurations for multireference calculations.[14–19]

The existence of additional solutions to the mean-field Hartree–Fock (HF) equations is intimately linked to symmetry-breaking in the wave function. As a mean-field approximation, the HF wave function is not required to conserve the symmetries of the exact Hamiltonian, including the spin-operators $\mathcal{S}^2$, $\mathcal{S}_z$, complex-conjugation, $\mathcal{K}$, or the time-reversal operator $\mathcal{T}$.[2,20] Enforcing particular symmetries ensures that the wave function retains certain well-defined quantum numbers, but restricts the variational freedom of the HF approximation: a choice often referred to as Löwdin's symmetry dilemma.[21] A HF solution that does not conserve a particular symmetry must always occur as a degenerate set of solutions related by the corresponding symmetry operator. These additional symmetry-broken solutions have been linked to the onset of strong electron correlation and provide reference states for methods such as projected Hartree–Fock (PHF),[22–24] or nonorthogonal configuration interaction (NOCI).[16]

While numerous developments have focused on locating multiple SCF solutions,[8,12,13,25–28] relatively little is known about the topology of the HF energy surface itself. The stability analysis popularised by Čížek and Paldus[29,30] allows a particular solution to be identified as a minimum, saddle point, or maximum, and allows downhill directions to be identified to characterise pathways.[31] However, the connectivity between stationary points, the general structure of the HF energy surface, and the effect of molecular symmetry on this surface remain largely unexplored. As a result, computational methods to locate multiple solutions generally rely on chemical intuition to determine which orbitals are associated with symmetry-breaking or electron excitations. Notable exceptions include the use of power series expansions of the HF energy,[26] the SCF metadynamics approach,[25] and linearisation of the SCF equations through Lie algebraic approaches.[27] In contrast, elucidating the topology of the SCF energy landscape itself promises a route towards more systematic approaches for locating multiple solutions.

In our opinion, there are two main reasons why the topology of the SCF energy has rarely been systematically investigated. Firstly, the SCF method is generally approached as an iterative procedure for identifying a self-consistent solution, rather than as an energy optimisation problem.[32,33] The combination of second-order optimisation methods[34–38] and Hessian-based stability analysis[29–31,39,40] has partially shifted this perspective, and provides a routine approach for finding true minima of the SCF energy (although there is no guarantee that the global minimum will be reached). Secondly, the SCF energy landscape is a relatively high-dimensional

[a)]Electronic mail: hugh.burton@chem.ox.ac.uk
[b)]Electronic mail: dw34@cam.ac.uk

surface with the number of free parameters determined by the number of occupied-virtual orbital rotations.[39] As a result, the SCF energy surface can only by fully visualised in minimal model systems,[41] while for larger molecules low-dimensional projections through the energy hypersurface are sometimes used.[26,42]

Analogous problems with high dimensionality are well known from studies of molecular energy landscapes, where the number of free parameters (atomic coordinates) grows linearly with the number of atoms in the system, and the number of stationary points grows exponentially.[43,44] On molecular energy landscapes, local minima represent stable molecular structures, while first-order saddle points correspond to transition states between distinct structures according to the Murrell-Laidler definition.[45] The pathways connecting successive local minima via first-order saddle points provide a coarse-grained representation of molecular rearrangements, and a wide variety of computational approaches for studying this connectivity have been established.[46]

In the present contribution, we investigate the topology of the real HF energy surface through the Energy Landscapes framework,[46] using analytic gradients and Hessians of the HF energy. The HF energy landscape is parameterised in terms of occupied-virtual orbital rotations, and stationary points correspond to individual solutions of the HF equations. The gradient alone is sufficient to locate local minima and the transition states that connect them through the hybrid eigenvector-following approach.[47–50] An analytic Hessian then allows the index (number of negative Hessian eigenvalues) of each stationary point to be classified, avoiding the need for numerical derivatives and the associated imprecision. This framework therefore allows us to understand how individual minima of the HF energy are connected and, for the first time, gain valuable insights into the topology of the SCF energy landscape itself.

In comparison to molecular potential energy surfaces, deriving analytic gradients and Hessians of the HF energy is complicated by the normalisation of the wave function and the invariance of a single Slater determinant with respect to occupied-occupied orbital rotations.[34] The relevant differential geometry of the Hartree–Fock energy is therefore summarised below. We have used these expressions to develop an interface between the Q-Chem electronic structure package[51] and the methodology for exploring energy landscapes encoded in our OPTIM[52] and PATHSAMPLE[53] programs. Results are then described for the H_4 model, which has proved to be a popular benchmark for investigating the existence of multiple HF solutions.[25,27,28] In particular, we investigate the effect of symmetry on the pathways connecting minima, and compare the electronic structure landscape for different geometries, basis sets, SCF potentials, and spin states.

II. EXPLORING THE HARTREE–FOCK ENERGY LANDSCAPE

A. Differential Geometry of the Hartree–Fock Energy

The differential geometry of the HF energy has been described in detail elsewhere (see Refs. 34 and 35), and so we will only summarise the details required in the current work. In what follows, we consider a $2n$-dimensional (nonorthogonal) spin-orbital basis $\{|\eta_\mu\rangle\}$ constructed as the direct product of an n-dimensional spatial basis $\{|\chi_\nu\rangle\}$ $(1 \leq \nu \leq n)$ and the two-component spin basis $\{|\alpha\rangle, |\beta\rangle\}$. We employ the nonorthogonal tensor notation defined by Head-Gordon *et al.* throughout.[54]

The HF wave function $|\Psi_{\text{HF}}\rangle$ for an N-electron system is defined as a single Slater determinant constructed from a set of occupied one-particle molecular orbitals $|\psi_i\rangle$.[55] The most general expansion of a molecular orbital (MO) takes the form

$$|\psi_i\rangle = \sum_{\mu}^{2n} |\eta_\mu\rangle C_{\cdot i}^{\mu\cdot}, \tag{1}$$

allowing each orbital to have both a spin-up (α) and spin-down (β) component.[2] We will only consider real HF wave functions represented by the domain $C_{\cdot i}^{\mu\cdot} \in \mathbb{R}$. Orthonormality of $|\Psi\rangle$ is ensured by the orbital coefficient constraint

$$\sum_{\mu}^{2n} C_{i\cdot}^{\cdot\mu} g_{\mu\nu} C_{\cdot j}^{\mu\cdot} = \delta_{ij}, \tag{2}$$

where $g_{\mu\nu} = \langle\eta_\mu|\eta_\nu\rangle$ is the metric tensor of the nonorthogonal spin-orbital basis functions. Due to the direct product structure of the spin-orbital basis, this metric takes the $2n \times 2n$ matrix form

$$\boldsymbol{g} = \begin{pmatrix} \mathbf{g} & \mathbf{0} \\ \mathbf{0} & \mathbf{g} \end{pmatrix}, \tag{3}$$

where $\mathbf{g}$ is the overlap matrix of the n-dimensional spatial basis. The HF energy is then defined in terms of the orbital coefficients as

$$\begin{aligned} E = V_{\text{nuc}} &+ \sum_{i}^{N}\sum_{\mu\nu}^{2n} C_{i\cdot}^{\cdot\mu} h_{\mu\nu} C_{\cdot i}^{\nu\cdot} \\ &+ \frac{1}{2}\sum_{ij}^{N}\sum_{\mu\nu\sigma\tau}^{2n} C_{i\cdot}^{\cdot\mu} C_{j\cdot}^{\cdot\sigma} \langle\mu\sigma||\nu\tau\rangle C_{\cdot i}^{\nu\cdot} C_{\cdot j}^{\tau\cdot}, \end{aligned} \tag{4}$$

where V_{nuc} is the nuclear repulsion, $h_{\mu\nu} = \langle\eta_\mu|\hat{h}|\eta_\nu\rangle$ are the one-electron integrals, and $\langle\mu\sigma||\nu\tau\rangle$ define the antisymmetrised two-electron integrals in the spin-orbital basis.[55]

Identifying HF solutions is equivalent to locating stationary points of the HF energy. However, satisfying the orthonormality condition requires that the HF energy is constrained to the hypersurface defined by Eq. (2). Furthermore, the HF energy depends on only the subspace spanned by the occupied orbitals and is invariant to occupied-occupied orbital

transformations.[55] Satisfying this invariance means that the orbital coefficients defining unique wave functions must be considered as points on a Grassmann manifold (see Refs. 34 and 56 for details). In the case of a single occupied orbital, this manifold reduces to a $2n$-dimensional hypersphere.[41]

For a given set of coefficients $\boldsymbol{C}$, any set of orbital coefficients $\widetilde{\boldsymbol{C}}$ satisfying the required constraints can be uniquely parameterised by the Thouless transformation[39]

$$\widetilde{\boldsymbol{C}}(\boldsymbol{\kappa}) = \boldsymbol{C} \exp \begin{pmatrix} \mathbf{0}_{\mathrm{O}} & -\boldsymbol{\kappa}^{\intercal} \\ \boldsymbol{\kappa} & \mathbf{0}_{\mathrm{V}} \end{pmatrix}, \tag{5}$$

where $\boldsymbol{\kappa}$ is an $(2n-N)\times N$ or $N_{\mathrm{V}}\times N_{\mathrm{O}}$ matrix with elements κ_{ai} defining local coordinates for the constraint surface at $\boldsymbol{C}$. Here we abbreviate the number of virtual and occupied molecular orbitals as N_{V} and N_{O}, and denote the corresponding square matrices of zeros as $\mathbf{0}_{\mathrm{V}}$ and $\mathbf{0}_{\mathrm{O}}$. The constrained gradient at the point $\boldsymbol{C}$ can then obtained in the local coordinate system as[35]

$$\left.\frac{\partial E}{\partial \kappa_{ai}}\right|_{\boldsymbol{\kappa}=\mathbf{0}} = 2\sum_{\mu\nu}^{2n} C_{a\cdot}^{\cdot\mu} F_{\mu\nu} C_{\cdot i}^{\nu\cdot} = 2F_{ai}, \tag{6}$$

where the Fock matrix in the spin-orbital basis is defined as[55]

$$F_{\mu\nu} = h_{\mu\nu} + \sum_{j}^{N}\sum_{\sigma\tau}^{2n} C_{j\cdot}^{\cdot\sigma} \langle \mu\sigma||\nu\tau\rangle C_{\cdot j}^{\tau\cdot}. \tag{7}$$

The analytic Hessian of the HF energy in this local coordinate system is given as[29,31]

$$\left.\frac{\partial^2 E}{\partial \kappa_{ai}\partial \kappa_{bj}}\right|_{\boldsymbol{\kappa}=\mathbf{0}} = 2\big(F_{ab}\delta_{ij} - F_{ij}\delta_{ab} + \langle aj||ib\rangle + \langle ab||ij\rangle\big), \tag{8}$$

where now the Fock matrix and two-electron integrals are represented in the MO basis defined by the coefficients $\boldsymbol{C}$. The exponential representation Eq. (5) generally leads to an infinite series for the gradient and Hessian that only simplifies to Eqs. (6) and (8) in the limit $\boldsymbol{\kappa} = \mathbf{0}$, as described by Ref. 35.

The HF parametrisation described above provides the most flexible form of real HF theory, corresponding to the generalised HF (GHF) approach.[20,57] While the flexibility of GHF can lead to lower energies, it also allows the wave function to break the symmetries corresponding to the $\mathcal{S}^2$ and $\mathcal{S}_z$ spin operators, and the time-reversal operator $\mathcal{T}$.[2] In contrast, constraining the wave function as an eigenfunction of $\mathcal{S}_z$ leads to the unrestricted HF (UHF) approach, where each electron occupies either an α or β orbital (i.e. different orbitals for different spins).[58] This constraint corresponds to splitting the orbitals into α and β sets defined as

$$|\psi_i\rangle = \sum_{\mu}^{n} |\alpha\rangle|\chi_\mu\rangle (C_\alpha)_{\cdot i}^{\mu\cdot} \tag{9a}$$

$$|\psi_{\bar{i}}\rangle = \sum_{\mu}^{n} |\beta\rangle|\chi_\mu\rangle (C_\beta)_{\cdot \bar{i}}^{\mu\cdot}, \tag{9b}$$

where the overbar indicates an index for a β orbital. The corresponding local coordinates and gradients are therefore restricted such that all non-spin-conserving occupied-virtual orbital transformations are ignored (i.e. $\kappa_{\bar{a}i} = \kappa_{a\bar{i}} = 0$). The addition of $\mathcal{S}^2$ and $\mathcal{T}$ symmetry leads to the restricted HF (RHF) approach where the α or β molecular orbitals must have the same spatial component, leading to the additional constraints $\boldsymbol{C}_\alpha = \boldsymbol{C}_\beta$ and $\kappa_{ai} = \kappa_{\bar{a}\bar{i}}$.[20]

In the current contribution, we will initially focus on the UHF formalism since this is the most familiar symmetry-broken HF approach applied in molecular systems. We then assess the connectivity of UHF solutions with different $\mathcal{S}_z$ eigenvalues by considering the GHF formalism. In the GHF approach we must handle the additional invariance to overall spin-rotations that lead to systematic zero Hessian eigenvalues of the GHF energy, as discussed in Appendix B. All the present calculations exploit a real HF wave function, although the computational framework can be extended in a straightforward way to complex HF formalisms.[59,60]

B. Distinguishing Hartree–Fock Stationary Points

Exploring the topology of the HF energy landscape requires a metric for distinguishing unique wave functions according to their orbital coefficients. One possibility includes the SCF electronic distance metric that compares the density matrices defined by the two states.[25] However, the wave function constraint produces a periodic hypersurface with every optimal HF density occurring as two stationary points $|\Psi_{\mathrm{HF}}^{+}\rangle$ and $|\Psi_{\mathrm{HF}}^{-}\rangle$ related by an overall sign change in the wave function. This pair of stationary points occur at different points on the electronic structure landscape, raising the possibility that solutions may be connected between their sign-related copies along different pathways. Therefore, while these sign permutations do not represent distinct physical wave functions, they are essential for understanding the topology of the electronic energy landscape.

To define a distance metric that distinguishes sign permutations of wave functions that produce the same electronic density, we first introduce the overlap between the wave functions $|{}^{x}\Psi_{\mathrm{HF}}\rangle$ and $|{}^{w}\Psi_{\mathrm{HF}}\rangle$ as

$${}^{xw}S = \langle {}^{x}\Psi_{\mathrm{HF}}|{}^{w}\Psi_{\mathrm{HF}}\rangle = \det\Big[({}^{x}\boldsymbol{C})^{\intercal}\boldsymbol{g}({}^{w}\boldsymbol{C})\Big]. \tag{10}$$

In the UHF case, this overlap factorises into the form

$${}^{xw}S = \det\Big[({}^{x}\boldsymbol{C}_\alpha)^{\intercal}\mathfrak{g}({}^{w}\boldsymbol{C}_\alpha)\Big]\det\Big[({}^{x}\boldsymbol{C}_\beta)^{\intercal}\mathfrak{g}({}^{w}\boldsymbol{C}_\beta)\Big]. \tag{11}$$

We then introduce the wave function d_Ψ and density d_ρ distances that compare the two sets of orbital coefficients as

$$d_\Psi(x,w) = 1 - {}^{xw}S, \tag{12a}$$

$$d_\rho(x,w) = 1 - |{}^{xw}S|. \tag{12b}$$

Since the overlap is bound in the range ${}^{xw}S \in [-1,1]$, both of these metrics are strictly positive (or zero). Using d_Ψ treats

the two sign permutations of the wave function as distinct points, while d_ρ ignores sign permutations and provides an equivalent to the SCF distance metric for comparing electronic densities.[25]

GHF wave functions with a zero Hessian eigenvalue exist as part of a one-dimensional continuum of solutions that are interconverted by a global spin rotation. We therefore consider stationary points that lie on the same continuum to be equivalent solutions. To identify the equivalence of two sets of coefficients, we apply a spin-rotation to maximise the spin-component of each wave function along a given axis before evaluating the overlap and distance metric defined above, as described in Appendix C.

C. Optimisation Techniques

An interface to Q-Chem already exists in the OPTIM program, providing access to a wide range of molecular geometry optimisation techniques. The same methodology was exploited to characterise the electronic structure landscape using a new interface, where the local variables of the $\boldsymbol{\kappa}$ matrix are employed together with analytic derivatives and (optionally) second derivatives. Working with the local variables enables us to use a non-redundant coordinate space, but requires the molecular orbital coefficients to be updated from the current reference at every optimisation step. All the optimisation routines produce a step in $\boldsymbol{\kappa}$ space, but the relation between $\boldsymbol{C}(\boldsymbol{\kappa})$ and $\boldsymbol{\kappa}$ via Eq. (5) is non-linear. We therefore applied every step in $\boldsymbol{\kappa}$ space to the current molecular orbital coefficients, and updated this reference. This approach allows us to deal only with steps in $\boldsymbol{\kappa}$ while the cumulative effect of the optimisation is tracked via the $\boldsymbol{C}$ coefficients.

The database of stationary points is saved in terms of the corresponding $\boldsymbol{C}$ values, and any subsequent calculations can be restarted from this set using new steps in $\boldsymbol{\kappa}$ space. This approach enables all the necessary derivatives to be evaluated for $\boldsymbol{\kappa} = \mathbf{0}$, but it required various modifications to the bookkeeping in OPTIM and PATHSAMPLE. For example, to calculate approximate integrated path lengths in $\boldsymbol{\kappa}$ space, we add the magnitudes of the steps along the steepest-descent pathways as the calculation proceeds, instead of storing all the intermediate configurations.

The optimisation techniques that were used to calculate minima, and the pathways that connect them via transition states, are equivalent to the usual formulation for geometry optimisation, aside for the changes noted above. These methods have been described in detail elsewhere,[46,61–63] and only a brief overview is provided here. Local minima were located using a customised L-BFGS[64] (limited memory Broyden,[65] Fletcher,[66] Goldfarb,[67] Shanno[68]) routine in OPTIM. Transition states were located using the gradient-only version of hybrid eigenvector-following,[47–50] following systematic perturbations in $\boldsymbol{\kappa}$ space applied to the molecular orbital coefficients corresponding to local minima. Here we define a transition state as a stationary point with Hessian index one.[45] Approximate steepest-descent paths were calculated to establish the connectivity using L-BFGS minimisation following small displacements parallel and antiparallel to the eigenvector corresponding to the unique negative Hessian eigenvalue. The Hessian index of every stationary point was verified using the eigenvalues of the analytic Hessian, since gradient-based methods can converge to higher index saddles, especially in configurations with high symmetry.[69]

We also searched systematically for index two saddle points, using an appropriately modified eigenvector-following approach with analytic second derivatives, previously employed to study the landscapes of structural glasses.[44,70] This method exploits the capability of the general eigenvector-following framework to walk uphill in a specified number of eigendirections. These searches were again initiated from the local minima following random perturbations applied through the $\boldsymbol{\kappa}$ coordinates.

The analytic Hessian was also used when accurate steepest-descent pathways were required to characterise catastrophes in the SCF landscape, as described in Section III C, and to investigate the downhill directions defined by specific Hessian eigenvectors for index 2 saddles. Here we employed the second order formulation of Page and McIver,[71] as implemented in OPTIM.

D. Visualising the SCF Landscape

The global organisation of the HF energy landscape can be visualised using disconnectivity graphs.[72,73] Each minimum corresponds to a vertical branch in the graph beginning at the corresponding energy. The branches are arranged on the horizontal axis to avoid crossings. At regularly spaced intervals in energy the minima merge if they can interconvert via any pathway that lies below the threshold. The landscape is therefore segregated into disjoint sets, or superbasins,[72] at each energy threshold. Hence we obtain a graphical view of how the landscape is organised, which faithfully preserves the barriers, and does not require an order parameter or a low-dimensional projection.

III. RESULTS: H_4 MODEL

The H_4 model has been extensively used to benchmark electronic structure methods and the existence of multiple HF solutions.[27,28,74,75] In particular, the square geometry (D_{4h}) provides an archetypal example of strong static electron correlation,[76–78] with a doubly degenerate RHF ground state and a number of symmetry-broken UHF solutions.[74] Furthermore, the H_4 model allows the reduction of molecular symmetry to be systematically studied by considering the distortion to rectangular, trapezoidal, or linear structures[76] (Figure 1). We first consider the UHF formalism with $\langle \mathcal{S}_z \rangle = 0$ using different SCF potentials, basis sets, and molecular structures. We then investigate the effect of changing the electronic spin state using the more flexible GHF approach in Section III D. Unless otherwise stated, we use the 3-21G basis set[79] with the HF potential. All energies are provided in atomic units of Hartrees (E_h).

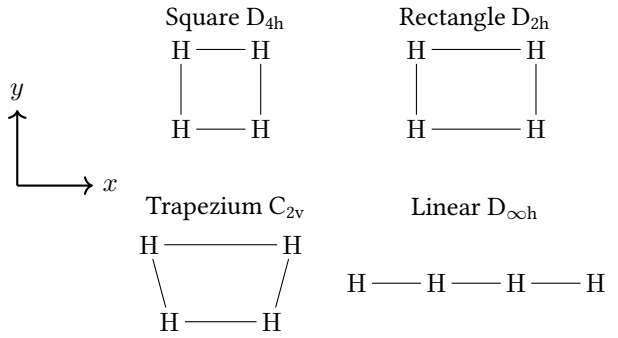

FIG. 1: Different structures considered for the H_4 model, with their corresponding spatial point groups.

Energy / E_h	Metric d_Ψ	Metric d_ρ
−1.785587	8	4
−1.790809	4	2
−1.792774	8	4
−1.803657	32	16
−1.893890	16	8

TABLE I: Degeneracies for the electronic densities corresponding to index-1 saddle points for square H_4 (side length 2 Å). Each pair of sign-permuted stationary points located on the UHF energy surfaces using the wave function distance d_Ψ corresponds to one distinct electron density when compared using density distance d_ρ.

A. Structure of the Landscape

We begin by considering the square H_4 structure with a side length of 2 Å using the UHF formalism with $\langle \mathcal{S}_z \rangle = 0$. In this geometry and spin state, the symmetry operations of the electronic wave function are given by the direct product group D_{4h}^T, which corresponds to $T \otimes D_{4h}$, where T is the group generated by the many-electron time-reversal operator. The structure of the D_{4h}^T group, and its irreducible representations, is described in Appendix A. Since the 3-21G basis set only includes s-type orbitals for hydrogen,[79] every wave function must be symmetric with respect to the σ_h mirror plane.

A total of 12 distinct minima were located on the UHF energy surface using the wave function distance metric d_Ψ, where each solution appears alongside its sign-permuted copy. These minima reduce to six distinct electronic densities when compared using the density distance metric d_ρ, forming two-fold and four-fold degenerate sets (Figure 2). Both sets of states correspond to a symmetry-broken wave function in the D_{4h}^T symmetry group. The two-fold degenerate global minima at $-1.999283\,E_h$ possess an antiferromagnetic structure, analogous to the symmetry-breaking predicted by Slater.[58] Together, this pair of solutions span the reducible representation $B_{1g}^+ \oplus A_{2g}^-$. In contrast, the local minima at $-1.974018\,E_h$ adopt an electronic structure where the spin-up and spin-down electrons localise on opposite sides of the square, and together they span the reducible representation $A_{1g}^+ \oplus B_{1g}^+ \oplus E_u^-$.

The unique minima on the UHF energy landscape are interconnected by a total of 68 index-1 saddles when sign permutations are explicitly considered using the wave function distance d_Ψ. These index-1 saddles correspond to 34 distinct electronic densities using the density distance d_ρ, and lead to six unique energies with degeneracies summarised in Table I.

The connectivity of minima via index-1 saddles allows the UHF energy landscape to be visualised as a disconnectivity graph (Figure 3). When electronic states are distinguished using d_Ψ, the landscape has a double-funnel structure where the minima are split into two groups of six, separated by a larger energy barrier (Figure 3a). In contrast, ignoring the sign permutations using the density distance d_ρ leads to a single-funnelled landscape (Figure 3b). The two funnels on the full HF energy landscape therefore correspond to wave functions related by sign permutations, where each funnel corresponds to the positive or negative copy of the exact ground-state wave function. Furthermore, all the minima are relatively close to the global minimum energy. The absence of high energy local minima suggests that mean-field HF excited states are likely to exist as higher-index saddles, and thus saddle-point optimisation algorithms will be required to identify such states.

Many of the index-1 pathways connect minima with the same energy, defining 20 symmetric degenerate rearrangements[80,81] of the canonical MOs that are illustrated in Figure 4. Each of these 20 transition states has an additional order-2 symmetry element that interconverts the two downhill pathways and the corresponding minima. The additional symmetries that appear in the transition state wave functions correspond to either a pure spatial symmetry operation, e.g. pathway (a), or the combination of a spatial operation and the time-reversal operator, e.g. pathways (b) and (c). These symmetric degenerate rearrangements demonstrate the strong influence of molecular symmetry on the structure of the SCF energy landscape through both the degeneracy of minima and the symmetries encoded by index-1 saddles.

For molecular energy landscapes, symmetric degenerate rearrangements must be associated with an additional spatial symmetry at the transition state that interconverts the two steepest-descent pathways and the product and reactant minima.[80,81] Asymmetric degenerate rearrangements are also possible in molecules,[82] where permutation-inversion isomers are linked by a transition state with no additional symmetry elements. Important examples arise for water clusters, where tunnelling splittings have been analysed in detail to provide a detailed experimental probe of the intermolecular forces and dynamics.[83–85] We discuss the analogue of asymmetric degenerate rearrangements of SCF minima using the linear structure of H_4 in Section III C.

In addition to the symmetric degenerate rearrangements, there are a further 48 non-degenerate pathways that connect minima with different energies. These non-degenerate pathways correspond to 24 distinct electronic densities that form 8-fold and 16-fold degenerate sets of HF solutions using the density distance d_ρ (see Table I). The corresponding rearrangements of the canonical MOs are illustrated in Figure 5. Notably, the only difference between the final minima (right) in path-

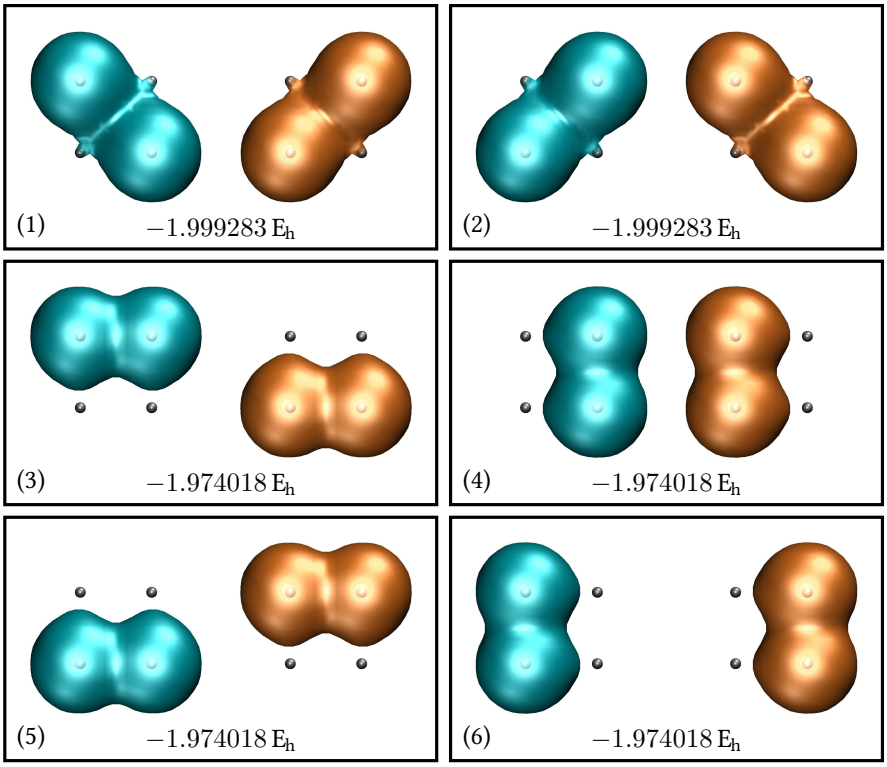

FIG. 2: Spin-up (blue) and spin-down (orange) densities associated with each minimum of the UHF energy surface for square H_4 (side length 2 Å). These minima occur in a two-fold degenerate set (1 and 2) and a four-fold degenerate set (3–6), with the minima in each set related by the D_{4h}^{T} symmetry operations. The minima within the pairs (1, 2), (3, 4) or (5, 6) are also interconverted by the reversal of spin-angular momentum generated by the time-reversal operator. Each density corresponds to two stationary points on the UHF energy surface, representing sign permutations of the corresponding wave function.

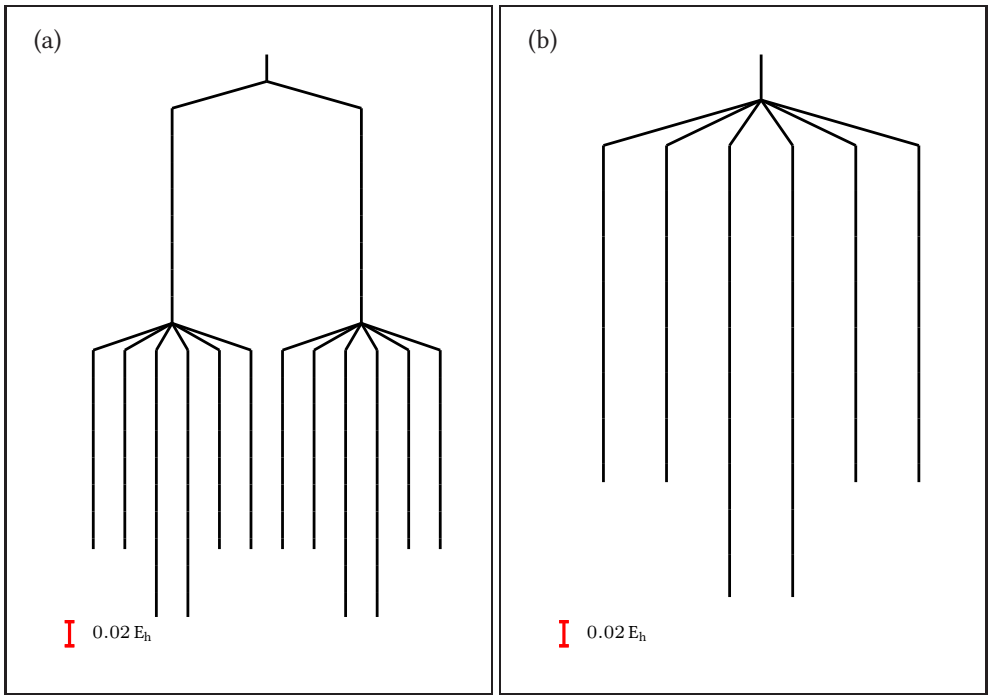

FIG. 3: Disconnectivity graphs for H_4 electronic states (3-21G) in the square geometry (side length 2 Å), where the stationary points are distinguished according to two different metrics, as defined in Eq. (12). (a) Wave function distance d_Ψ. (b) Density distance d_ρ.

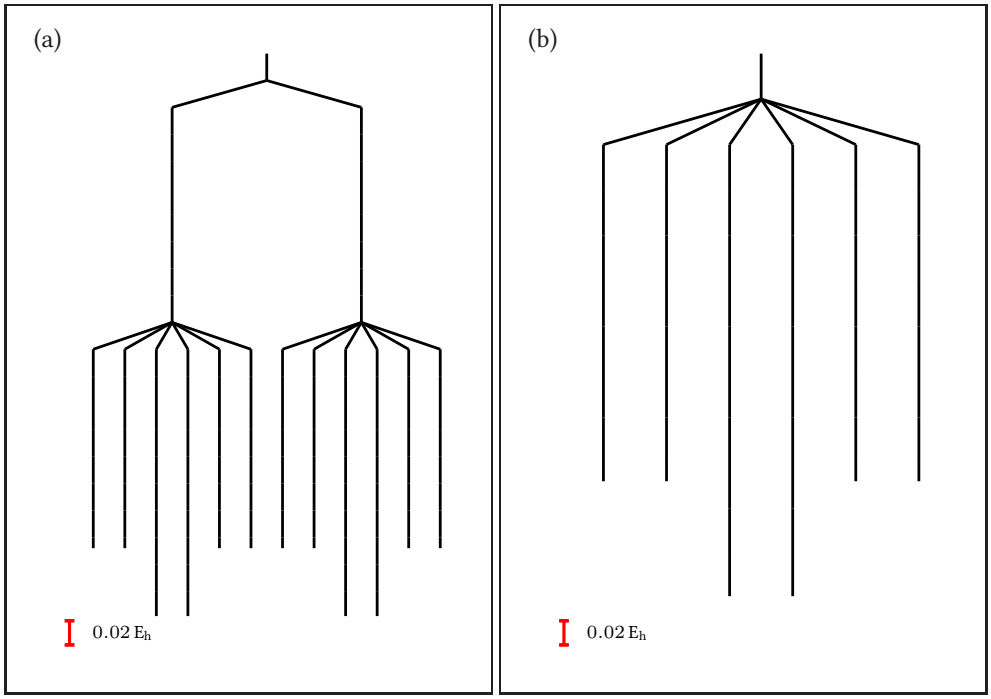

FIG. 4: Illustration of symmetric degenerate rearrangements between symmetry-related minima for square H_4 (side length 2 Å). For each state, the occupied α and β orbitals correspond to the left and right columns, respectively. Every transition state gains an additional order-2 symmetry operation that must interconvert the minima at the end points of the corresponding pathway. The C_2^+ and C_2^- rotations coincide with the $y = x$ and $y = -x$ axes, respectively (see Figure 1).

ways (d) and (e) is the introduction of a minus sign in one spin-up MO, demonstrating the importance of considering distinct sign permutations. No new symmetry elements occur at the transition state of these non-degenerate rearrangements. The symmetries of the MOs must therefore be conserved along the full pathway because the gradient transforms as the totally symmetric irreducible representation.[86–90] In addition to the σ_h reflection, the transition state MOs for the lower energy pathway (d) are only symmetric with respect to the combined operation $\mathcal{T}C_2^y$ (where the C_2^y rotation axis coincides with the y-axis), and this symmetry is conserved along the full pathway. In contrast, the higher-energy pathway (e) conserves no symmetry elements, except the σ_h reflection enforced by the 3-21G basis set.

The lack of symmetry in the transition state MOs for pathway (e) leads to a 16-fold degenerate set of HF solutions. Since every wave function using s-type orbitals must be symmetric with respect to reflection in the plane of the molecule, a degeneracy of 16 is the largest possible for a wave function in the D_{4h}^T symmetry group. The corresponding HF wave functions therefore conserve the fewest number of symmetry elements, in contrast to the minima and other index-1 saddles on the landscape. The existence of these fully symmetry-broken saddle points emphasises the fact that symmetry breaking does not always lower the ground-state energy, but can also occur throughout the energy spectrum. Instead, the lack of symmetry along non-degenerate rearrangements implies that the most symmetry-broken HF solutions are likely to be index-1 saddles rather than minima whenever there are at least two minima with different energies.

Finally, we identified a total of 164 index-2 saddles using the wave function distance d_Ψ at the square geometry (side length 2 Å), reducing to 82 distinct electronic densities using d_ρ. Index-2 saddles can represent important HF wave functions on the SCF energy landscape. For example, the spin-symmetry-pure RHF global minimum at this square geometry is an index-2 saddle on the UHF energy landscape. The steepest-descent pathways along the two eigenvectors of the Hessian corresponding to the negative eigenvalues are found to connect degenerate minima that are related by the spin-flip operation. Since the two steepest-descent pathways for each downhill eigenvector are related by time-reversal symmetry, the index-2 saddle itself must exhibit this symmetry element, enforcing a restricted closed-shell wave function. This index-2 saddle is itself doubly degenerate, with one saddle connecting the pairs of minima (1,2) and (3,4) from Figure 2, and the symmetry-related partner connecting the pairs of minima (1,2) and (5,6).

B. Dependence on the Level of Theory

The SCF approach can be applied at various levels of accuracy using different theoretical approximations. For example, increasing the size of the spin-orbital basis set increases the accuracy towards the exact HF limit. Alternatively, applying the SCF approximation through density functional theory (DFT) allows electron-electron interactions to be represented

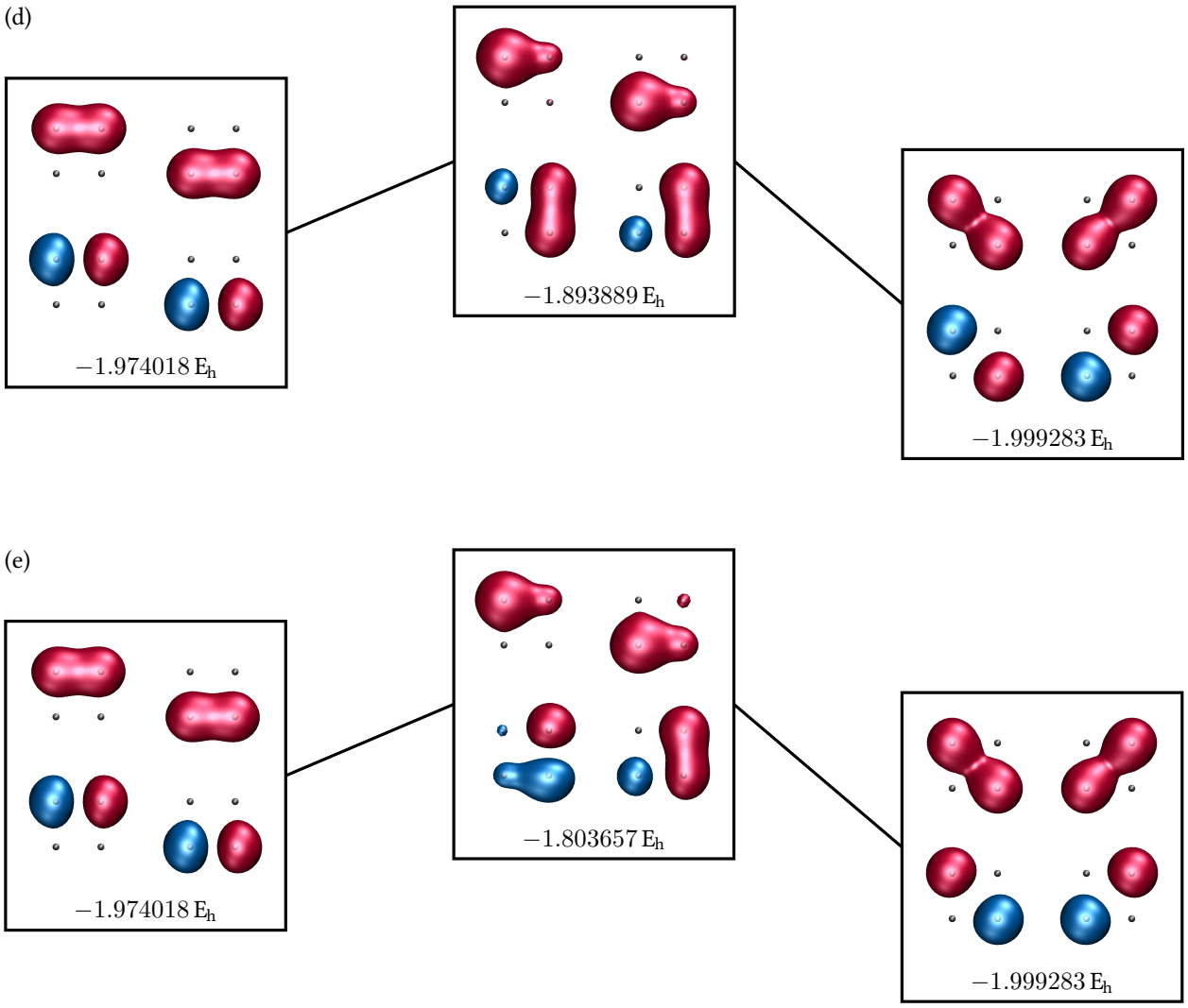

FIG. 5: Illustration of non-degenerate rearrangements that interconvert HF minima with different energies. The MOs do not gain any new order-2 symmetries at the transition state, and all symmetries must be conserved along the full pathway.

through an exchange-correlation functional. If the exact functional were known, then the Kohn–Sham (KS-DFT) approach would allow the exact energy to be identified in a single-particle SCF representation.[91] Additional SCF solutions are common in KS-DFT and are also known to form symmetry broken wave functions.[75,92] In this Section, we investigate how the topology of the SCF energy landscape depends on the level of theory applied by considering UHF theory using the 3-21G and aug-cc-pVDZ[93] basis sets, and we compare the HF and B3LYP[94,95] potentials for a consistent basis set (3-21G).

Disconnectivity graphs for the square structure ($\langle \mathcal{S}_z \rangle = 0$; side length 2 Å) using these different levels of theory are compared in Figure 6. The number and degeneracies of SCF energy minima is the same in each case, with the same connectivity via index-1 saddles. While the number of minima and index-1 saddles is identical for the 3-21G and aug-cc-pVDZ basis sets, there is a reduction in the number of index-2 saddles for the aug-cc-pVDZ basis set (Table II). There is further reduction in the number of index-1 and index-2 saddles for the B3LYP exchange-correlation potential. Therefore, although the basis set or SCF potential leaves the general structure and symmetry of the landscape unchanged, it can change the relative energies of stationary points and cause certain solutions to disappear. The disappearance of solutions using different levels of theory is analogous to the case of Coulson–Fischer points in HF theory,[96] where changes in relative components of the energy for different molecular structures can cause HF solutions to coalesce and vanish.[41,75,97]

The topology of the SCF energy landscape at different levels of theory provides insights into the origins of multiple SCF solutions. Firstly, the similarity between the disconnectivity graphs for different basis sets demonstrates that symmetry-breaking and multiple solutions arise from the single determinant wave function constraint, rather than the particular contributions to the energy. Viewing the space of single determinants parametrised by the Thouless transformation[39] as a subspace of the exact wave function manifold, additional HF solutions emerge from the way that the HF constraint surface

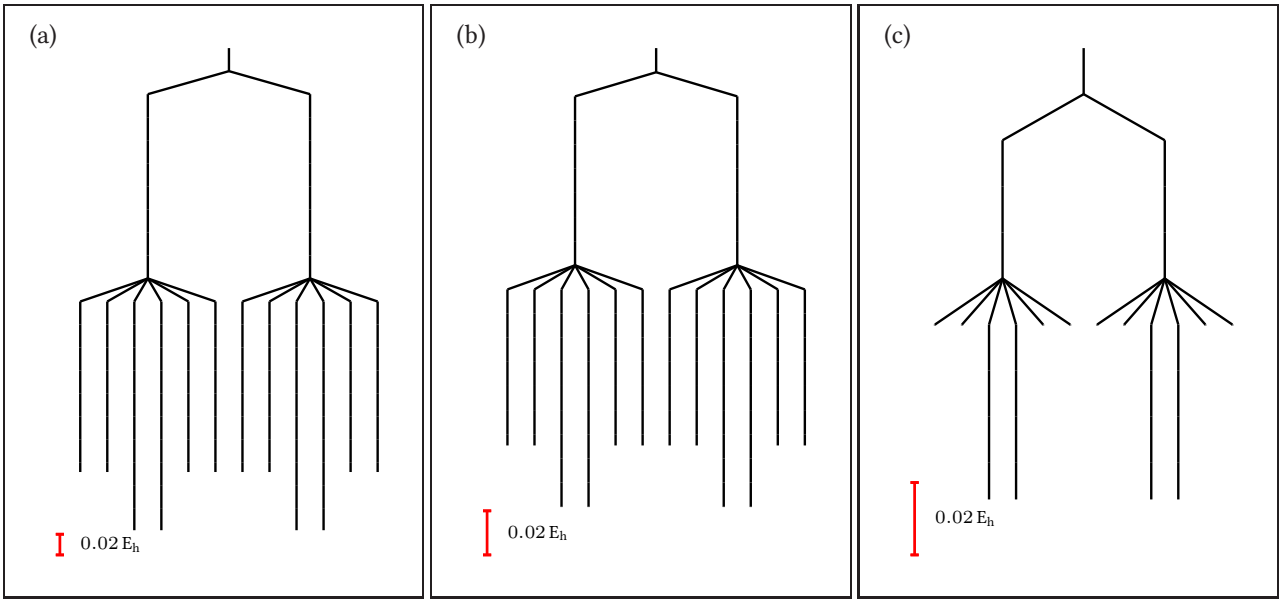

FIG. 6: Disconnectivity graphs for H_4 electronic SCF states in the square geometry (side length 2 Å) using different levels of theory. Sign permutations are considered as distinct solutions using the wave function distance d_Ψ. (a) HF using the 3-21G basis set. (b) HF using the aug-cc-pVDZ basis set. (c) B3LYP-DFT using the 3-21G basis set.

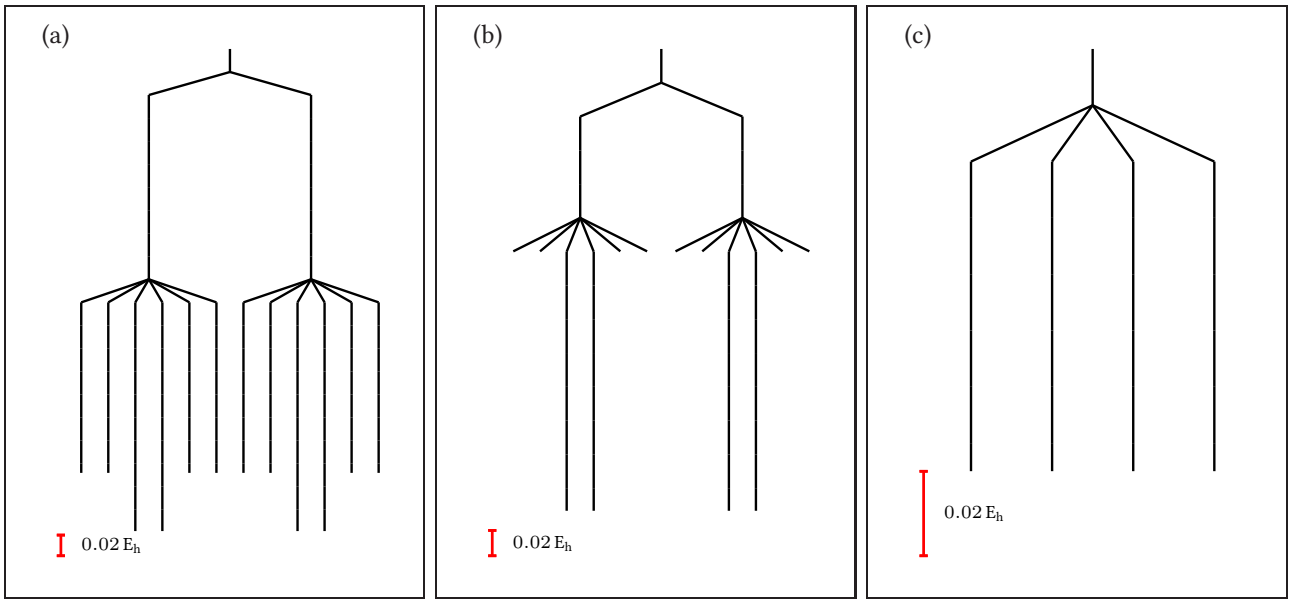

FIG. 7: Disconnectivity graphs for H_4 electronic SCF states (3-21G) in square geometries with various side lengths. Sign permutations are considered as distinct solutions using the wave function distance d_Ψ. (a) Side length 2.0 Å. (b) Side length 1.5 Å. (c) Side length 1.0 Å.

projects the exact energy landscape.[98] This perspective reveals how multiple local minima can occur in HF theory, while the exact energy has strictly *one* minimum.

Secondly, the change in relative energies using different basis sets or the B3LYP potential demonstrates how the exact energy landscape underlying the single determinant approximation affects the topology of SCF solutions. Notably we find fewer solutions overall using the B3LYP functional, with a reduction in the number of index-1 and index-2 saddles. The index-1 saddles that are lost between HF and B3LYP correspond to pathways (a) and (d), leaving only one pathway between each set of degenerate solutions. This reduction in the number of solutions implies that the SCF energy landscape is more convex using the B3LYP functional than for pure HF theory. In turn, a more convex landscape suggests that the B3LYP surface provides a better approximation to the

Basis	Theory	Minima	Index-1	Index-2
3-21G	HF	12	68	164
	B3LYP	12	28	84
aug-cc-pVDZ	HF	12	68	132

TABLE II: Total number of minima and index-1 saddle points of the SCF energy for alternative basis sets using HF or B3LYP potentials. Sign permutations of solutions are considered as distinct stationary points using the wave function distance d_Ψ.

exact electronic energy surface (with one global minimum), as might be expected if the exchange-correlation functional provides a better representation of the electron-electron interactions. One might interpret this result as a vindication of the DFT approach.

C. Effect of the Molecular Structure

It is well known that the number of HF solutions can change for different molecular structures. For example, solutions to the HF equation may disappear along a molecular binding curve when the eigenvalue structure of the HF Hessian changes, leading to so-called HF instability thresholds.[99,100] These thresholds are often associated with the emergence of a symmetry-broken HF wave function, for example at the Coulson–Fischer point in H_2 where two UHF minima spontaneously emerge from the ground-state RHF solution as the bond length increases.[58,96] In this Section, we visualise how changes in molecular structure affect the topology of the corresponding UHF solutions in H_4 with $\langle \mathcal{S}_z \rangle = 0$.

Geometry	Point Group	Minima	Index-1	Index-2
Square 2.0 Å	D_{4h}	12	68	164
Square 1.5 Å	D_{4h}	12	20	52
Square 1.0 Å	D_{4h}	4	8	20
Rectangle	D_{2h}	12	68	164
Trapezium	C_{2v}	12	68	172
Linear	$D_{\infty h}$	2	4	12

TABLE III: Total number of minima and index-1 or index-2 saddle points of the HF energy for various geometries. Sign permutations of solutions are considered as distinct stationary points using the wave function distance d_Ψ.

Consider the symmetric stretch of the square geometry using the 3-21G basis set. The H_4 wave function is highly multireference in character at the stretched configuration, but becomes more single-reference at shorter bond lengths, although the RHF ground state remains doubly degenerate throughout. The total number of minima, index-1 saddles, and index-2 saddles for square side-lengths of 2.0, 1.5 and 1.0 Å, compared using the the wave function distance d_Ψ. is given in Table III, and the corresponding disconnectivity graphs are plotted in Figure 7. There is a clear reduction in the number of HF solutions as the side length shortens, with more higher-energy saddles appearing at longer side lengths than minima. However, the degeneracy of solutions and the symmetry of the landscape is conserved, as expected, since the molecular structure remains in the D_{4h} point group throughout. Similar to the results in Section III B, the smaller number of solutions at shorter side lengths can be interpreted as an indication that the HF energy provides a better approximation to the exact energy landscape at these geometries.

The HF energies for the low-energy minima, index-1 saddles, and index-2 saddles along the symmetric square stretch are shown in Figure 8. There is a general increase in the HF energies of index-1 saddles relative to minima, and index-2 saddles relative to index-1 saddles, providing further evidence that there are no high-energy local minima on the SCF energy landscape. Furthermore, as the side length decreases, solutions that disappear are seen to coalesce and vanish at two-fold pair-annihilation points and three-fold confluence points along the binding curve.[41,99] The disappearance of the four-fold degenerate local minima occurs at three-fold coalescence points corresponding to cusp catastrophes, where one minimum coalesces with two index-1 saddle points to leave a single index-1 saddle point (see Appendix D). When these HF solutions disappear, complex-analytic extensions can be constructed using the recently developed holomorphic HF approach[41,74,101] and its KS-DFT counterpart.[97]

The symmetry of H_4 can be systematically reduced by distorting the molecule from the square D_{4h} structure to the rectangular D_{2h} geometry, the trapezium C_{2v} geometry, or a linear chain $D_{\infty h}$ (Figure 1). A rectangular structure was constructed by stretching two opposing bonds by 0.1 Å, while the trapezium structure was constructed by symmetrically stretching one bond by 0.2 Å. The linear chain was constructed with interatomic spacings of 0.875 Å, corresponding to the equilibrium distance for an equally-spaced chain. The number of minima, index-1 saddles, and index-2 saddles identified using the wave function distance d_Ψ is given in Table III, and the corresponding disconnectivity graphs are shown in Figure 9.

Square 2.0 Å Energy / E_h	Square D_{4h}^T	Rectangle D_{2h}^T	Trapezium C_{2v}^T
−1.974018	$A_{1g}^+ \oplus B_{1g}^+ \oplus E_u^-$	$A_g^+ \oplus B_{3u}^-$	$A_1^+ \oplus A_1^-$
		$A_g^+ \oplus B_{2u}^-$	$A_1^+ \oplus B_1^-$
−1.999283	$B_{1g}^+ \oplus A_{2g}^-$	$A_g^+ \oplus A_{1g}^-$	$A_1^+ \oplus B_1^-$

TABLE IV: Representations spanned by the degenerate minima from the square 2.0 Å geometry as the H_4 molecule is distorted into a rectangular and trapezoidal structure. The four-fold degenerate set splits into two two-fold degenerate sets, represented on different rows.

For the rectangular and trapezium structures, the distortion from the square geometry is relatively small and the number of minima and index-1 saddles remains the same (Table III). However, the number of index-2 saddles increases in the trapezium structure. These additional solutions were found to vanish as the structure is distorted back towards the square. In both cases, the global minima remain doubly degenerate, although the degeneracy of the local minima is

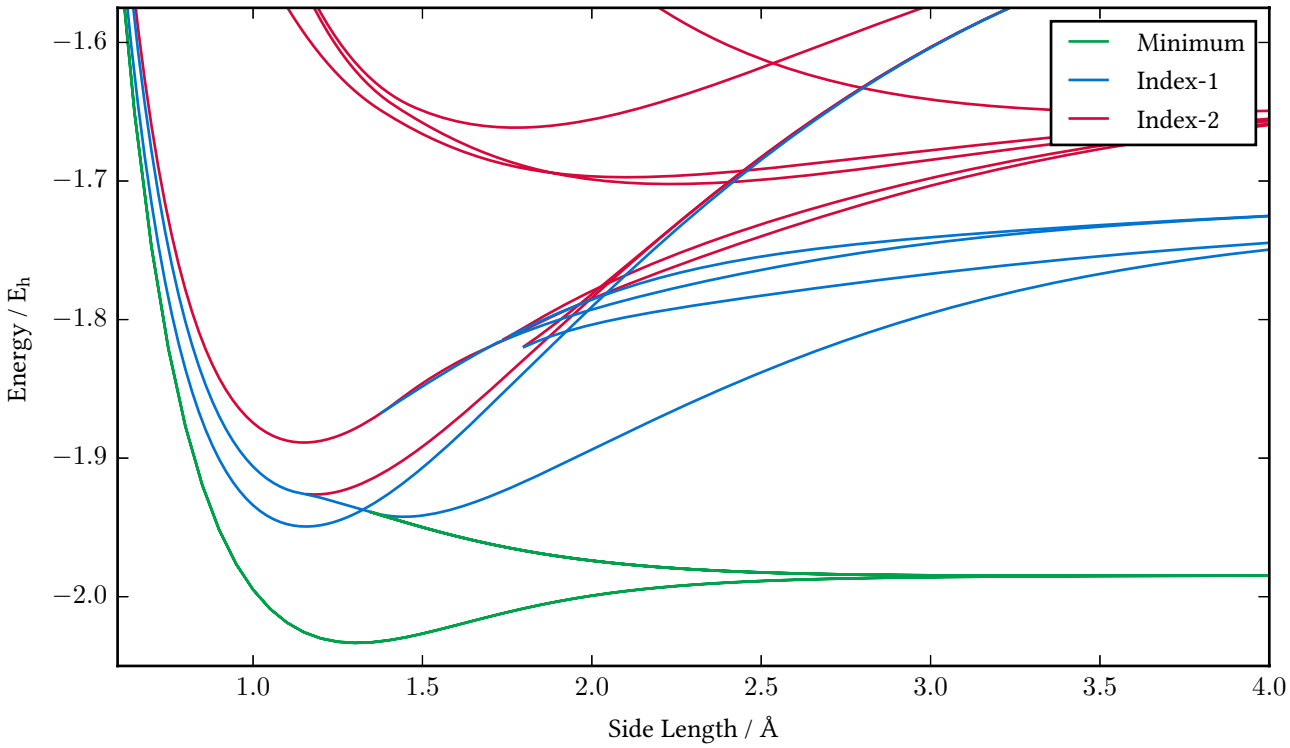

FIG. 8: HF solutions along the square H_4 stretch, and their classification as either minima, index-1 or index-2 saddles.

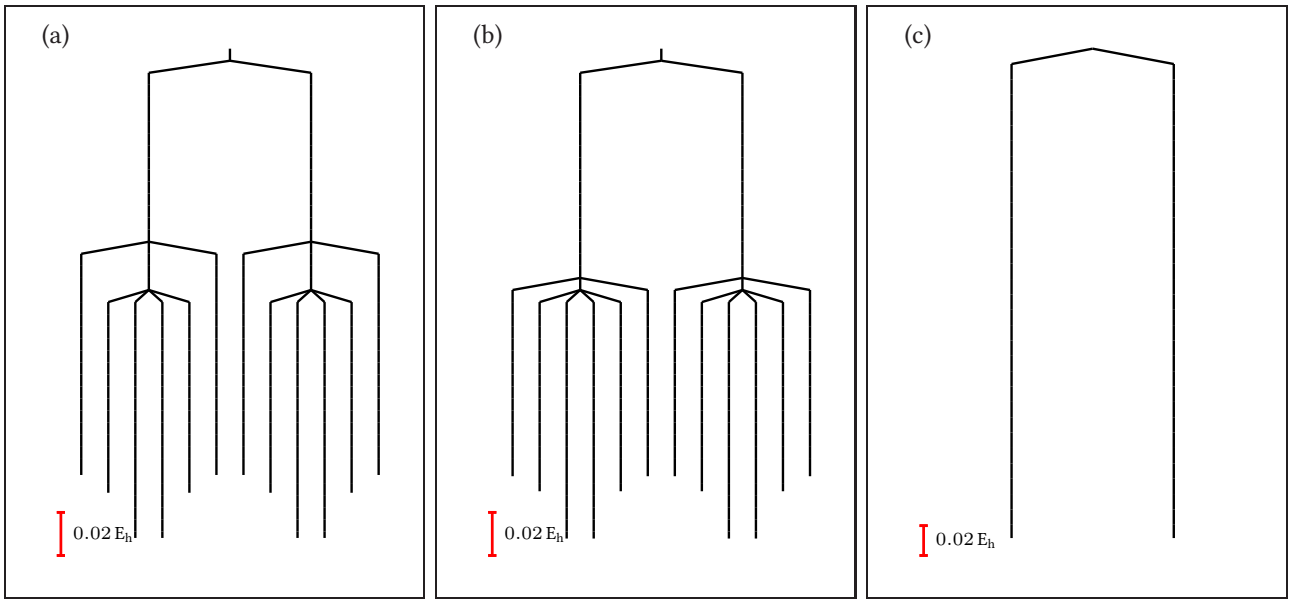

FIG. 9: Disconnectivity graphs for H_4 electronic states using the 3-21G basis set, distinguished according to wave function distance d_Ψ from Eq. (12). (a) Rectangle. (b) Trapezium. (c) Linear, equilibrium bond length 0.875 Å.

reduced from four in the square geometry to two sets of two-fold degenerate minima in the rectangle and trapezium. The representations spanned by the minima are summarised in Table IV, where the time-reversal extensions of the D_{2h} and C_{2v} spatial groups are introduced as D^T_{2h} and C^T_{2v}, respectively. The broken spatial symmetry is reflected in the disconnectivity graphs (Figure 9) where we find that the transition states connecting the new two-fold degenerate sets of minima also become slightly higher in energy. However, the double-funnel structure is retained throughout, suggesting that this property

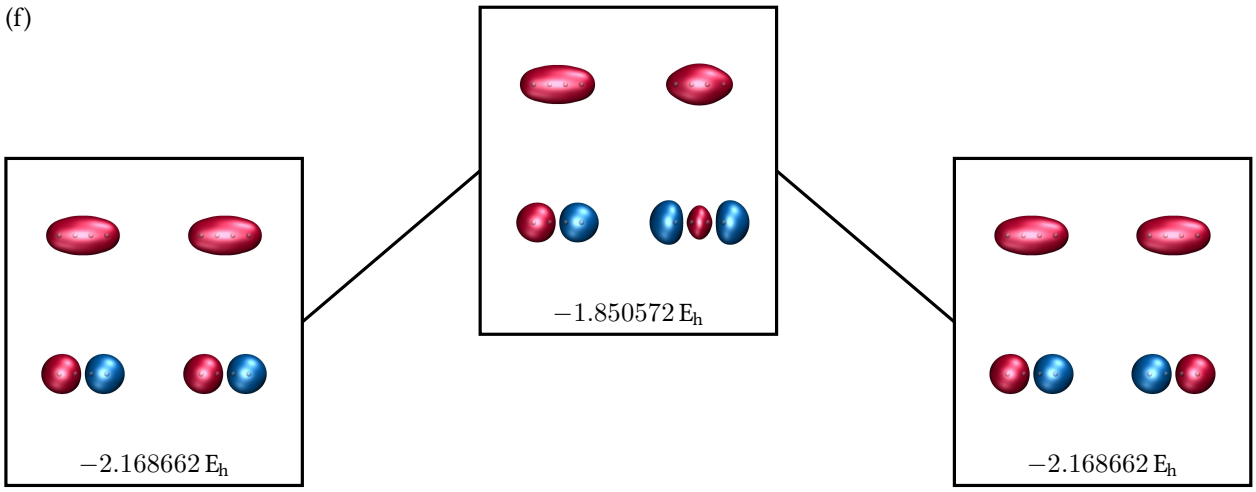

FIG. 10: Illustration of the asymmetric degenerate rearrangements that interconvert the sign-permuted global HF minima in the equilibrium linear chain structure. The MOs do not gain any new order-2 symmetries at the transition state, indicating that sign-permuting the overall wave function is not a physical symmetry of the Hamiltonian.

is a fundamental feature of the SCF energy landscape for H_4.

Finally, we consider the equilibrium linear structure with an equal interatomic spacing of 0.875 Å. Only two minima can be identified using the wave function distance d_Ψ, corresponding to positive and negative sign permutations of the RHF global minimum. With no HF symmetry-broken solutions, this structure would conventionally be considered to have a single-reference exact wave function with no strong static correlation effects. The absence of static correlation is directly reflected in the disconnectivity graph (Figure 9c), where the two sign-permuted minima are connected by a four-fold degenerate set of index-1 saddle points. As above, the reduction in the number of minima and higher-index saddle points relative to the square geometry suggests that, for the linear structure, the SCF landscape is more convex and provides a better approximation to the exact electronic energy surface.

The equilibrium linear structure is the only geometry where we find two sign-permuted minima directly connected by an index-1 saddle point, leading to a degenerate rearrangement. The canonical MOs along this rearrangement are illustrated in Figure 10. Although the initial and final minima only differ by a sign change in the second occupied β orbital, there is no other *physical* symmetry operation that can interconvert these two minima. As a result, the transition state does not gain an additional order-2 symmetry element and the pathways correspond to an asymmetric degenerate rearrangement. Order-2 symmetries, which must appear at transition states for symmetric degenerate rearrangements, therefore correspond to physical symmetries of the Hamiltonian, and introducing a sign-change to the wave function is not such a symmetry. Furthermore, the fact that this transition state is spin-symmetry broken directly reflects the failure of single determinant wave functions for describing single excitations.

D. Comparing Spin States

Wave functions in the UHF approximation are constrained as eigenfunctions of the $\mathcal{S}_z$ operator with corresponding eigenvalues given by the quantum number m_s. Since H_4 has a total of four electrons, this constraint gives rise to distinct energy landscapes with $m_s = 0$, 1, or 2. In this section, we consider the $m_s = 1$ and 2 landscapes for the square H_4 structure at a side length of 2 Å, for comparison with the $m_s = 0$ results, above.

With $m_s = 1$, an eight-fold degenerate set of global minima can be identified using the wave function distance metric. This eight-fold degeneracy arises from a spatial symmetry breaking in the wave function where the single β electron localises on one of the four hydrogen atoms. The various symmetric copies of these degenerate minima are interconnected by a total of 44 index-1 saddles, with energies and degeneracies summarised in Table V. The corresponding pathways all correspond to degenerate orbital rearrangements (see Section SI A), although since the number of α and β electrons differ, any symmetric degenerate rearrangements can only occur via two-fold spatial symmetry operations.

In contrast, only two minima, corresponding to mutual sign-permutations, were identified with $m_s = 2$, along with an eight-fold degenerate set of index-1 saddles (Table V). The existence of only two minima representing the same electronic density reflects the predominantly single-reference nature of this high-spin configuration, in common with the $m_s = 0$ linear structure considered above. More generally, this single-reference character is shared with other high-spin configurations and provides the motivation behind the use of high-spin reference orbitals in the spin-flip family of methods.[102] Furthermore, since all the "1s" molecular orbitals are occupied in the $m_s = 2$ global minimum, the orbital rearrangement pathways must involve excitations to the 2s orbitals (see Section SI B), leading to the relatively high transition state energy.

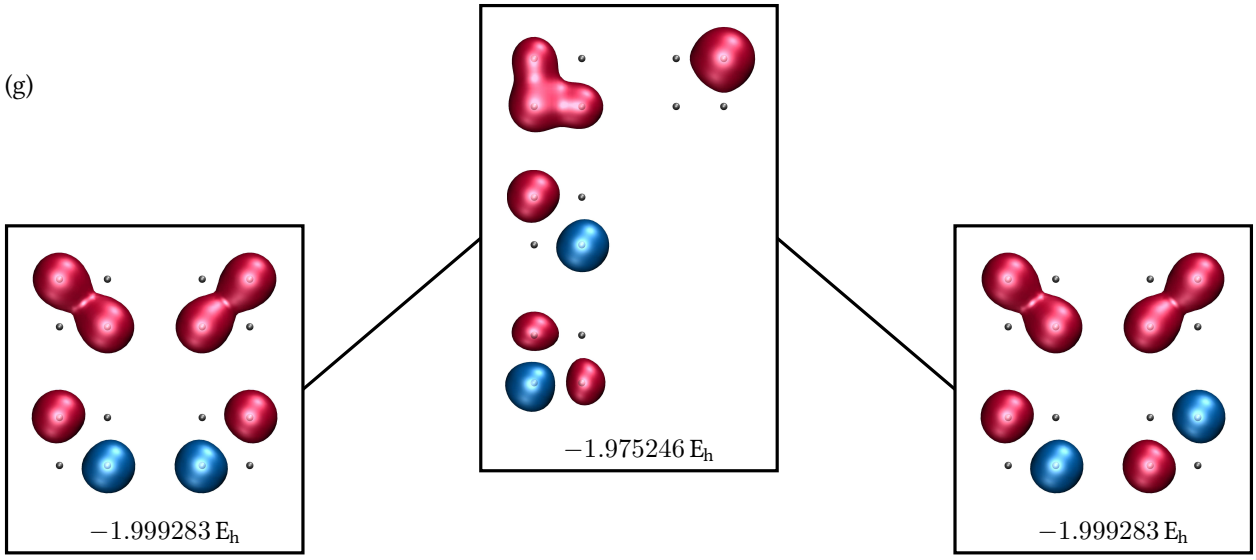

FIG. 11: Illustration of GHF pathway connecting $m_s = 0$ sign-permuted minima via an index-1 saddle with $|m_s| = 1$. For each state, high-spin (α) and low-spin (β) orbitals occupy the left and right columns respectively.

	$m_s = 1$		$m_s = 2$	
	Energy / E_h	Degen.	Energy / E_h	Degen.
Minima	−1.975 246	8	−1.946 698	2
Index-1	−1.893 446	8	−0.849 013	8
	−1.787 340	8		
	−1.783 818	4		
	−1.782 694	8		
	−1.773 859	4		
	−1.718 130	4		
	−1.665 124	8		

TABLE V: Energy and degeneracy of minima and index-1 saddle points for the $m_s = 1$ and 2 UHF energy of square H_4 (3-21G) with side-length 2 Å. Sign-permutations are considered as distinct points using the wave function distance d_Ψ.

Energy / E_h	m_s	UHF Index	GHF Index
−1.999 283	0	0	0
−1.974 018	0	0	2
−1.893 889	0	1	2
−1.803 657	0	1	3
−1.792 774	0	1	3
−1.790 809	0	1	4
−1.785 587	0	1	3
−1.975 246	1	0	1
−1.893 446	1	1	2
−1.787 340	1	1	3
−1.783 818	1	1	4
−1.782 694	1	1	4
−1.773 859	1	1	4
−1.718 130	1	1	4
−1.665 124	1	1	4
−1.946 698	2	0	3
−0.849 013	2	0	7

TABLE VI: Change in the Hessian index between the UHF and GHF formalisms for UHF minima and index-1 saddles located with each m_s value.

Identifying connections between UHF solutions for different m_s spin states requires the removal of the $\mathcal{S}_z$-symmetry constraint on the wave function and the application of the GHF formalism. Although the symmetry of the GHF landscape ensures that UHF solutions must also be stationary points in the GHF representation, the Hessian index is unlikely to be conserved. This change in index arises as new pathways between stationary points become possible with a more flexible wave function, as noted previously for complex wave functions.[103] Furthermore, the presence of zero Hessian eigenvalues for solutions with $\langle \mathcal{S}^2 \rangle \neq 0$ results in a one-dimensional continuum of solutions defined by a global spin rotation (see Appendix B). As a result, spin-flip pairs of solutions with $m_s = 0$ fall on the same GHF continuum, as do spin-collinear stationary points with non-zero m_s values related by a change in sign (e.g. $m_s = \pm 1$). We consider stationary points that fall on the same continuum as equivalent solutions, and identify them using the approach described in Appendix C.

Table VI illustrates the change in Hessian index of the UHF minima and index-1 saddles in the GHF formalism for the square 2.0 Å structure. Only the $m_s = 0$ UHF global minima remain as minima in the GHF formalism, while all the other UHF stationary points correspond to index-1 (or higher) GHF saddles. The degeneracy of the $m_s = 0$ minima is reduced from four-fold to two-fold because spin-flip pairs of UHF solutions become part of the same stationary GHF continuum, and there are two such continua related by a sign-permutation of the wave function. These two continua are connected by the eight spatial symmetry-broken index-1 saddles corresponding

to the UHF $m_s = 1$ global minima. Each of these index-1 stationary points also has $\langle \mathcal{S}^2 \rangle \neq 0$ and forms a one-dimensional GHF continuum with $|m_s| = 1$. No true non-collinear GHF minima or index-1 saddles were identified, as expected since H_4 would not generally be considered a spin-frustrated system. The $m_s = 0$ minima at $-1.999283\,\mathrm{E_h}$ therefore represent the global minima of the real HF energy surface.

The orbital rearrangement between the two degenerate global $m_s = 0$ minima via an $|m_s| = 1$ index-1 saddle is illustrated in Figure 11. While GHF solutions have been shown to connect different UHF spin states along molecular binding curves,[60,104] we believe this is the first time that such states have been connected in the orbital parametrisation space. It seems non-intuitive that the $m_s = 0$ solutions can be connected by pathways mediated by $|m_s| = 1$ index-1 saddles. However, the only way to "physically" introduce the sign-change that interconverts the two $m_s = 0$ minima is to apply the one-electron time-reversal operator $\hat{\tau}$ (see Appendix A) twice to any single electron (since $\hat{\tau}^2 = -\mathcal{I}$). The intermediate state, where $\hat{\tau}$ has been applied only once, reverses the spin of this electron and hence gives rise to a state with $|m_s| = 1$. We have also identified the same connectivity between $m_s = 0$ and $|m_s| = 1$ states in the linear equilibrium geometry of H_4, where the GHF global minimum is a closed-shell RHF solution. The consistency of these observations suggests that there may be more fundamental and systematic connections between spin-states, and we will investigate these in future work.

IV. DISCUSSION AND CONCLUSIONS

In this contribution, we have employed the Energy Landscapes framework to systematically understand solutions of the real SCF equations. Using H_4 as a prototypical model, we have directly probed the structure and general properties of the SCF energy landscape. In particular, we have found that the real SCF energy surface generally forms a double-funnel structure, with minima in each funnel related by a sign-permutation of the overall wave function. This double-funnelled organisation has important consequences for the development of single-determinant optimisation techniques.

Firstly, locating one of the lowest energy solutions will not be challenging for methods such as basin-hopping global optimisation,[105–107] which can successfully treat far more complex landscapes. One application of basin-hopping to SCF optimisation has recently been introduced by Dong *et al.* using the Lie algebraic approach.[108] The funnelled structure of the SCF landscape also explains why methods such as SCF metadynamics[25] and Geometric Direct Minimisation[34] can locate the global minimum.

Secondly, the absence of high-energy local minima provides a guiding principle for developing methods to locate mean-field SCF approximations to electronic wave functions. In particular, it seems very likely that these high-energy SCF solutions are all high-index saddle points of the SCF energy, particularly when symmetry constraints on the wave function are removed. This observation encourages further development of excited-state optimisation approaches that systematically search for stationary points regardless of their Hessian index, for example squared-gradient minimisation,[12] state-targeted energy projection,[13] or variance-based approaches.[109] However, we note that square-gradient or variance optimisation can lead to numerous nonstationary points where the gradient is non-zero, but is instead a null-eigenvector of the Hessian with a zero eigenvalue.[44,110] The effect of these nonstationary points on wave function optimisation could be systematically assessed by investigating the square-gradient SCF landscape itself. Alternatively, these higher-energy saddles can be identified efficiently using the modified eigenvector-following approach developed for structural glasses,[44,70] which we employed in the present work to locate index-2 saddles.

Using the square H_4 structure, we have systematically characterised the pathways connecting distinct minima via index-1 saddle points. In particular, we found that pathways connecting degenerate minima that are not related by a sign permutation correspond to symmetric degenerate rearrangements, where the index-1 saddle point gains an additional order-2 symmetry element, which interconverts the two downhill directions.[80,81] On the other hand, non-degenerate pathways that connect minima with different energies lead to index-1 saddles with a greater degree of symmetry breaking. As a result, the most symmetry-broken SCF solutions are often index-1 saddles on non-degenerate pathways, emphasising that symmetry breaking does not always lower the energy.[21] High-energy excited-state SCF solutions are therefore likely to suffer from severe symmetry breaking, and post-HF symmetry-restoration will often be required to recover physically interpretable wave functions. Here we suggest that projection-after-variation schemes such as NOCI[16,17] or the variance-based Half-Projected σ-SCF[111] (variation-after-projection) offer the most reliable approaches to avoid variational collapse.

Using the $m_s = 0$ UHF landscape, we have demonstrated how changing the basis set, SCF potential, and the molecular structure affects the topology of the SCF energy landscape. Changing any of these factors can alter the relative energies of SCF solutions or cause certain solutions to disappear in an analogous way to the Coulson–Fischer point in H_2.[96] When the SCF approximation is qualitatively correct, the electronic energy landscape appears to have a small number of minima and saddle points, with a convex structure; when the single-determinant approximation fails in the presence of static correlation, a large number of minima and higher-index saddles can be found.

Improving the theoretical approximation by increasing the size of the basis set or introducing a DFT exchange-correlation functional also appears to reduce the total number of stationary points. However, the general double-funnelled structure of the SCF landscape, and the pathways between minima, are largely unaffected. As a result, the topology of the SCF energy landscape is heavily influenced by the nature of the single-determinant wave function constraint, and the way that this constrained subspace projects the exact electronic energy landscape. Further understanding the relationship between approximate wave function subspaces and the ex-

act wave function constraint surface may allow the merits of different ground and excited state approximations to be better understood, and we will investigate this possibility in future work. We also intend to extend the analysis to larger molecules. The SCF and analytic hessian calculations scale as $\mathcal{O}(n^4)$ and $\mathcal{O}(n^5)$, respectively. The optimisation procedures we have employed to locate stationary points are routinely applied to molecular systems with several thousand degrees of freedom. In practice the bottleneck for SCF landscape analysis may be the growth of the number of stationary points with the number of degrees of freedom. In molecular systems this growth is expected to be exponential,[43,44] and the SCF solutions show a similar scaling.[98,112]

Finally, by extending our description to the GHF approximation, we have identified the connectivity between UHF solutions with different m_s values In the GHF formalism, solutions with $\langle \mathcal{S}^2 \rangle \neq 0$ form a continuum of stationary points related by global spin rotations. We have found only one global (continuum) minimum in H_4, corresponding to the $m_s = 0$ ground-state, with sign-permutations connected across $|m_s| = 1$ index-1 saddles. The existence of only one distinct minimum and index-1 saddle suggests that the GHF energy surface is also more convex than the corresponding UHF landscape, as expected with the more flexible wave function. This observed convexity supports the "single minimum hypothesis" of Hammes-Schiffer and Anderson where, if the GHF method is accurate, it should have only one minimum.[57] These authors proposed that this single GHF minimum would then aid the development of *ab initio* molecular dynamics simulations by avoiding the artifical discontinuities that occur when multiple RHF or UHF states cross. Our approach to understanding the HF energy surface now allows the convexity of GHF to be systematically investigated in larger systems, and we intend to explore this direction in the future.

Although we have only considered the model problem of H_4 using the real HF approximation, we believe that our results lay the foundations for further investigations of electronic structure theory from an energy landscape perspective. In particular, extending our approach to complex orbitals would allow the relationship between strong correlation and complex RHF solutions to be investigated.[59,60] Furthermore, comparing the landscapes of correlated methods with the HF energy surface opens a new avenue for understanding the breakdown of HF theory in the presence of strong correlation effects.

ACKNOWLEDGEMENTS

HGAB thanks Alex Thom for stimulating discussions throughout the development of this work and New College, Oxford for funding through the Astor Junior Research Fellowship. DJW gratefully acknowledges the EPSRC for financial support.

Appendix A: Group Theory of H_4 Model

Interpreting symmetric degenerate rearrangement[80,81] pathways in H_4 with $\langle \mathcal{S}_z \rangle = 0$ requires an understanding of the underlying symmetries of the HF energy landscape. In general, the symmetry groups that must be considered in the HF approximation include spatial point group Ω, and the direct product group $S \otimes T$, where S is the spin-rotation group and T is the time-reversal group.[2] Since we are only considering the UHF case, the spin of our wave function is collinear by construction and must be invariant to all spin-rotations around a common axis. Furthermore, in the absence of a magnetic field, there is no preferred orientation for this common spin axis, usually denoted the z axis. The only way in which UHF wave function can break symmetry is therefore through operations that belong to the direct-product group of the spatial symmetry operators $\mathcal{R}$ and the time-reversal operator $\mathcal{T}$.

A detailed overview of the time-reversal operator for general spin states can be found in Ref. 113 and in the Appendix of Ref. 114. The action of $\mathcal{T}$ on a single-fermion state is described as odd due to the relationship $\mathcal{T}^2 = -E$, where E is the identity operator. However, the many-electron form of $\mathcal{T}$ is given by the direct product of the one-electron time-reversal operators $\hat{\tau}(i)$ that act on an electron i to give

$$\mathcal{T} = \bigotimes_{i=1}^{N} \hat{\tau}(i). \tag{A1}$$

Considering the many-electron form of $\mathcal{T}^2$, given by

$$\mathcal{T}^2 = \bigotimes_{i=1}^{N} \hat{\tau}(i)^2 = (-1)^N E, \tag{A2}$$

we find that the action of $\mathcal{T}$ is odd for a system with an odd number of electrons, and even otherwise. Since H_4 with $\langle \mathcal{S}_z \rangle = 0$ has an even number of electrons, we only need to consider the direct product group of the even time-reversal group $T = \{E, \mathcal{T}\}$ and the spatial point group operations $\mathcal{R} \in \Omega$, defining the set $\{\mathcal{R}, \mathcal{T}\mathcal{R} \,|\, \mathcal{R} \in \Omega\}$, which clearly has order $2|\Omega|$. We denote this extended form of the spatial point group using the superscript notation Ω^{T}.

The molecular point group of square H_4 is D_{4h}. Noting that $\mathcal{T}$ commutes with all the operations $\mathcal{R}$, and that the character of $\mathcal{T}$ can take two values $\chi(\mathcal{T}) = \pm 1$, we can use the relationship $\chi(\mathcal{T}\mathcal{R}) = \chi(\mathcal{T})\chi(\mathcal{R})$ to construct the character table for the direct product group D_{4h}^{T}, as shown in Table VII. Each irreducible representation Γ in D_{4h} maps onto two irreducible representations Γ^+ and Γ^- in D_{4h}^{T} with a positive or negative character under $\mathcal{T}$, respectively, giving a total of 20 irreducible representations in the direct-product group.

Doubling the number of irreducible representations in a direct-product group Ω^{T} is also important for the construction of symmetry-restored spin-pure wave functions using nonorthogonal configuration interaction (NOCI) expansions of symmetry-broken HF solutions.[16] For a spin-contaminated $m_s = 0$ determinant (i.e. one that is not an eigenfunction of

D_{4h}^{T}	E	$2C_4$	C_4^2	$2C_2$	$2C_2'$	i	$2S_4$	σ_h	$2\sigma_v$	$2\sigma_d$	$\mathcal{T}$	$2\mathcal{T}C_4$	$\mathcal{T}C_4^2$	$2\mathcal{T}C_2$	$2\mathcal{T}C_2'$	$\mathcal{T}i$	$2\mathcal{T}S_4$	$\mathcal{T}\sigma_h$	$2\mathcal{T}\sigma_v$	$2\mathcal{T}\sigma_d$
A_{1g}^{+}	1	1	1	1	1	1	1	1	1	1	1	1	1	1	1	1	1	1	1	1
A_{2g}^{+}	1	1	1	−1	−1	1	1	1	−1	−1	1	1	1	−1	−1	1	1	1	−1	−1
B_{1g}^{+}	1	−1	1	1	−1	1	−1	1	1	−1	1	−1	1	1	−1	1	−1	1	1	−1
B_{2g}^{+}	1	−1	1	−1	1	1	−1	1	−1	1	1	−1	1	−1	1	1	−1	1	−1	1
E_{g}^{+}	2	0	−2	0	0	2	0	−2	0	0	2	0	−2	0	0	2	0	−2	0	0
A_{1u}^{+}	1	1	1	1	1	−1	−1	−1	−1	−1	1	1	1	1	1	−1	−1	−1	−1	−1
A_{2u}^{+}	1	1	1	−1	−1	−1	−1	−1	1	1	1	1	1	−1	−1	−1	−1	−1	1	1
B_{1u}^{+}	1	−1	1	1	−1	−1	1	−1	−1	1	1	−1	1	1	−1	−1	1	−1	−1	1
B_{2u}^{+}	1	−1	1	−1	1	−1	1	−1	1	−1	1	−1	1	−1	1	−1	1	−1	1	−1
E_{u}^{+}	2	0	−2	0	0	−2	0	2	0	0	2	0	−2	0	0	−2	0	2	0	0
A_{1g}^{-}	1	1	1	1	1	1	1	1	1	1	−1	−1	−1	−1	−1	−1	−1	−1	−1	−1
A_{2g}^{-}	1	1	1	−1	−1	1	1	1	−1	−1	−1	−1	−1	1	1	−1	−1	−1	1	1
B_{1g}^{-}	1	−1	1	1	−1	1	−1	1	1	−1	−1	1	−1	−1	1	−1	1	−1	−1	1
B_{2g}^{-}	1	−1	1	−1	1	1	−1	1	−1	1	−1	1	−1	1	−1	−1	1	−1	1	−1
E_{g}^{-}	2	0	−2	0	0	2	0	−2	0	0	−2	0	2	0	0	−2	0	2	0	0
A_{1u}^{-}	1	1	1	1	1	−1	−1	−1	−1	−1	−1	−1	−1	−1	−1	1	1	1	1	1
A_{2u}^{-}	1	1	1	−1	−1	−1	−1	−1	1	1	−1	−1	−1	1	1	1	1	1	−1	−1
B_{1u}^{-}	1	−1	1	1	−1	−1	1	−1	−1	1	−1	1	−1	−1	1	1	−1	1	1	−1
B_{2u}^{-}	1	−1	1	−1	1	−1	1	−1	1	−1	−1	1	−1	1	−1	1	−1	1	−1	1
E_{u}^{-}	2	0	−2	0	0	−2	0	2	0	0	−2	0	2	0	0	2	0	−2	0	0

TABLE VII: Character table for the direct product group D_{4h}^{T}. Each irreducible representation Γ in D_{4h} maps onto two irreducible representations Γ^{+} and Γ^{-} with a positive or negative character under $\mathcal{T}$, respectively. The order of the group is 32.

$\hat{S}^2$), it is known that building linear combinations with the spin-flip partner function can reduce spin-contamination by providing two new wave functions that are a mixture of the exact states with odd S or even S, respectively. The direct-product group Ω^{T} explains this approach, since the character of an $m_s = 0$ wave function under the operation of $\mathcal{T}$ is given by $(-1)^S$.[113] States with even S must therefore form a basis for an irreducible representation Γ^{+}, while states with odd S form a basis for the corresponding irreducible representation Γ^{-}. For example, the two degenerate minima at the square geometry (see Section III A) transform together as the reducible representation $B_{1g}^{+} \oplus A_{2g}^{-}$, and thus their linear combination yields approximate singlet $^1B_{1g}$ and triplet $^3A_{2g}$ NOCI states. These symmetries underpin the partial spin-restoration achieved in the Half-Projected Hartree–Fock approach,[23,115] although to the best of our knowledge it has not previously been explained in this explicit group theoretical form.

Appendix B: Zero Hessian Eigenvalues for Overall Spin-Rotation

When considering the energy landscape for GHF wave functions, we need to take into account the degeneracy of states with respect to an overall spin-rotation. For wave functions satisfying $\mathcal{S}_z$ symmetry, this transformation corresponds to a rotation of the spin-collinearity axis. More generally, overall spin-rotations leave the energy unchanged and can result in Hessian eigenvectors with zero eigenvalues.[116] To understand the effect of these eigenvectors, we require an analytic form in the $\boldsymbol{\kappa}$-vector space that we use to locally parameterise the HF energy landscape.

A general spin-rotation of angle θ about an axis $\hat{\boldsymbol{n}}$ is represented in the two-component spinor basis as

$$\boldsymbol{R}(\hat{\boldsymbol{n}}, \theta) = \exp\left(\mathrm{i}\frac{\theta}{2}\hat{\boldsymbol{n}} \cdot \boldsymbol{\sigma}\right), \tag{B1}$$

where the vector $\boldsymbol{\sigma} = (\boldsymbol{\sigma}_x, \boldsymbol{\sigma}_y, \boldsymbol{\sigma}_z)$ contains the Pauli spin matrices. From the form of these spin matrices, only rotations around the y-axis retain real orbitals, giving the transformation in the direct-product spin-orbital basis as

$$\boldsymbol{R}(\hat{\boldsymbol{y}}, \theta) = \begin{pmatrix} \boldsymbol{I}_n \cos\frac{\theta}{2} & \boldsymbol{I}_n \sin\frac{\theta}{2} \\ -\boldsymbol{I}_n \sin\frac{\theta}{2} & \boldsymbol{I}_n \cos\frac{\theta}{2} \end{pmatrix}, \tag{B2}$$

where $\boldsymbol{I}_n$ is the n-dimensional identity matrix. Therefore, overall spin rotations in real GHF lead to (at most) one systematic zero eigenvalue of the Hessian, and spin rotations around the x or z axes can be ignored.

The action of a y-axis spin rotation leads to a rotation of the atomic spin-orbital basis and transforms the molecular orbital coefficients $\boldsymbol{C}$ as

$$\boldsymbol{C}(\theta) = \boldsymbol{R}_n(\hat{\boldsymbol{y}}, \theta)\boldsymbol{C}, \tag{B3}$$

where $\boldsymbol{C} = \boldsymbol{C}(0)$ and

$$\boldsymbol{R}_n(\hat{\boldsymbol{y}}, \theta) = \begin{pmatrix} \boldsymbol{I}_n \cos\frac{\theta}{2} & \boldsymbol{I}_n \sin\frac{\theta}{2} \\ -\boldsymbol{I}_n \sin\frac{\theta}{2} & \boldsymbol{I}_n \cos\frac{\theta}{2} \end{pmatrix}. \tag{B4}$$

However, it is the corresponding transformation in the $\boldsymbol{\kappa}$ space of non-redundant orbital rotations [see Eq. (5)] that is required. The relevant $\boldsymbol{\kappa}$ matrix can be identified by solving

$$\boldsymbol{R}_n(\hat{\boldsymbol{y}}, \theta)\boldsymbol{C} = \boldsymbol{C}\exp\begin{pmatrix} \boldsymbol{0}_{\mathrm{O}} & -\boldsymbol{\kappa}^{\intercal} \\ \boldsymbol{\kappa} & \boldsymbol{0}_{\mathrm{V}} \end{pmatrix}. \tag{B5}$$

Pre-multiplying by $\boldsymbol{C}^{\intercal}\boldsymbol{g}$ and exploiting the orthogonality $\boldsymbol{C}^{\intercal}\boldsymbol{g}\boldsymbol{C} = \boldsymbol{I}$ yields

$$\exp\begin{pmatrix} \boldsymbol{0}_{\mathrm{O}} & -\boldsymbol{\kappa}^{\intercal} \\ \boldsymbol{\kappa} & \boldsymbol{0}_{\mathrm{V}} \end{pmatrix} = \boldsymbol{C}^{\intercal}\boldsymbol{g}\boldsymbol{R}_n(\hat{\boldsymbol{y}}, \theta)\boldsymbol{C}. \tag{B6}$$

Representing the orbital coefficient matrix in terms of both α/β and occupied/virtual subblocks as

$$\boldsymbol{C} = \begin{pmatrix} \boldsymbol{C}_{\alpha}^{\mathrm{O}} & \boldsymbol{C}_{\alpha}^{\mathrm{V}} \\ \boldsymbol{C}_{\beta}^{\mathrm{O}} & \boldsymbol{C}_{\beta}^{\mathrm{V}} \end{pmatrix} \tag{B7}$$

and the overlap tensor in direct-product form (3) gives

$$\boldsymbol{C}^\intercal \mathbf{g} = \begin{pmatrix} (\boldsymbol{C}_\alpha^{\mathrm{O}})^\intercal \mathbf{g}_n & (\boldsymbol{C}_\beta^{\mathrm{O}})^\intercal \mathbf{g}_n \\ (\boldsymbol{C}_\alpha^{\mathrm{V}})^\intercal \mathbf{g}_n & (\boldsymbol{C}_\beta^{\mathrm{V}})^\intercal \mathbf{g}_n. \end{pmatrix} \tag{B8}$$

Hence we obtain

$$\exp\begin{pmatrix} \mathbf{0}_{\mathrm{O}} & -\boldsymbol{\kappa}^\intercal \\ \boldsymbol{\kappa} & \mathbf{0}_{\mathrm{V}} \end{pmatrix} = \begin{pmatrix} \cos\frac{\theta}{2}\left(\boldsymbol{S}^{\mathrm{OO}}_{\alpha\alpha} + \boldsymbol{S}^{\mathrm{OO}}_{\beta\beta}\right) + \sin\frac{\theta}{2}\left(\boldsymbol{S}^{\mathrm{OO}}_{\alpha\beta} - \boldsymbol{S}^{\mathrm{OO}}_{\beta\alpha}\right), & \cos\frac{\theta}{2}\left(\boldsymbol{S}^{\mathrm{OV}}_{\alpha\alpha} + \boldsymbol{S}^{\mathrm{OV}}_{\beta\beta}\right) + \sin\frac{\theta}{2}\left(\boldsymbol{S}^{\mathrm{OV}}_{\alpha\beta} - \boldsymbol{S}^{\mathrm{OV}}_{\beta\alpha}\right) \\ \cos\frac{\theta}{2}\left(\boldsymbol{S}^{\mathrm{VO}}_{\alpha\alpha} + \boldsymbol{S}^{\mathrm{VO}}_{\beta\beta}\right) + \sin\frac{\theta}{2}\left(\boldsymbol{S}^{\mathrm{VO}}_{\alpha\beta} - \boldsymbol{S}^{\mathrm{VO}}_{\beta\alpha}\right), & \cos\frac{\theta}{2}\left(\boldsymbol{S}^{\mathrm{VV}}_{\alpha\alpha} + \boldsymbol{S}^{\mathrm{VV}}_{\beta\beta}\right) + \sin\frac{\theta}{2}\left(\boldsymbol{S}^{\mathrm{VV}}_{\alpha\beta} - \boldsymbol{S}^{\mathrm{VV}}_{\beta\alpha}\right) \end{pmatrix} \tag{B9}$$

where the overlap matrices are defined as e.g. $\boldsymbol{S}^{\mathrm{OV}}_{\alpha\beta} = (\boldsymbol{C}^{\mathrm{O}}_\alpha)^\intercal \mathfrak{g} \boldsymbol{C}^{\mathrm{V}}_\beta$. Exploiting the expanded orthogonality constraint

$$\begin{pmatrix} \boldsymbol{S}^{\mathrm{OO}}_{\alpha\alpha} + \boldsymbol{S}^{\mathrm{OO}}_{\beta\beta}, & \boldsymbol{S}^{\mathrm{OV}}_{\alpha\alpha} + \boldsymbol{S}^{\mathrm{OV}}_{\beta\beta} \\ \boldsymbol{S}^{\mathrm{VO}}_{\alpha\alpha} + \boldsymbol{S}^{\mathrm{VO}}_{\beta\beta}, & \boldsymbol{S}^{\mathrm{VV}}_{\alpha\alpha} + \boldsymbol{S}^{\mathrm{VV}}_{\beta\beta} \end{pmatrix} = \begin{pmatrix} \boldsymbol{I}_{\mathrm{O}} & \mathbf{0}_{\mathrm{OV}} \\ \mathbf{0}_{\mathrm{VO}} & \boldsymbol{I}_{\mathrm{V}} \end{pmatrix}, \tag{B10}$$

where $\mathbf{0}_{\mathrm{OV}}$ and $\mathbf{0}_{\mathrm{VO}}$ are rectangular matrices of zeros, allows Eq. (B9) to be simplified as

$$\exp\begin{pmatrix} \mathbf{0}_{\mathrm{O}} & -\boldsymbol{\kappa}^\intercal \\ \boldsymbol{\kappa} & \mathbf{0}_{\mathrm{V}} \end{pmatrix} = \begin{pmatrix} \cos\left(\frac{\theta}{2}\right)\boldsymbol{I}_{\mathrm{O}} + \sin\frac{\theta}{2}\left(\boldsymbol{S}^{\mathrm{OO}}_{\alpha\beta} - \boldsymbol{S}^{\mathrm{OO}}_{\beta\alpha}\right) & -\sin\frac{\theta}{2}\left(\boldsymbol{S}^{\mathrm{VO}}_{\alpha\beta} - \boldsymbol{S}^{\mathrm{VO}}_{\beta\alpha}\right)^\intercal \\ \sin\frac{\theta}{2}\left(\boldsymbol{S}^{\mathrm{VO}}_{\alpha\beta} - \boldsymbol{S}^{\mathrm{VO}}_{\beta\alpha}\right) & \cos\left(\frac{\theta}{2}\right)\boldsymbol{I}_{\mathrm{V}} + \sin\frac{\theta}{2}\left(\boldsymbol{S}^{\mathrm{VV}}_{\alpha\beta} - \boldsymbol{S}^{\mathrm{VV}}_{\beta\alpha}\right) \end{pmatrix}, \tag{B11}$$

where we have used $\left(\boldsymbol{S}^{\mathrm{VO}}_{\alpha\beta} - \boldsymbol{S}^{\mathrm{VO}}_{\beta\alpha}\right)^\intercal = -\left(\boldsymbol{S}^{\mathrm{OV}}_{\alpha\beta} - \boldsymbol{S}^{\mathrm{OV}}_{\beta\alpha}\right)$.

To represent the spin-rotation as a $\boldsymbol{\kappa}$ transformation, we seek a relationship between Eq. (B11) and the exponential form of an orthogonal matrix given by[117]

$$\exp\begin{pmatrix} \mathbf{0}_{\mathrm{O}} & -\boldsymbol{\kappa}^\intercal \\ \boldsymbol{\kappa} & \mathbf{0}_{\mathrm{V}} \end{pmatrix} = \begin{pmatrix} \boldsymbol{V}\cos(\boldsymbol{\Sigma})\boldsymbol{V}^\intercal + (\boldsymbol{I}_{\mathrm{O}} - \boldsymbol{V}\boldsymbol{V}^\intercal) & -\boldsymbol{V}\sin(\boldsymbol{\Sigma})\boldsymbol{U}^\intercal \\ \boldsymbol{U}\sin(\boldsymbol{\Sigma})\boldsymbol{V}^\intercal & \boldsymbol{U}\cos(\boldsymbol{\Sigma})\boldsymbol{U}^\intercal + (\boldsymbol{I}_{\mathrm{V}} - \boldsymbol{U}\boldsymbol{U}^\intercal) \end{pmatrix}, \tag{B12}$$

where $\boldsymbol{\kappa} = \boldsymbol{U}\boldsymbol{\Sigma}\boldsymbol{V}^\intercal$ is a compact singular value decomposition, and $\boldsymbol{U}$, $\boldsymbol{\Sigma}$ and $\boldsymbol{V}^\intercal$ have dimensions $N_V \times N_V$, $N_V \times N_V$, and $N_V \times N_O$, respectively.

The OV and VO blocks of Eq. (B11) and Eq. (B12) are very similar in form, but a direct analogy fails in the OO and VV blocks. However, occupied-occupied and virtual-virtual transformations leave the overall energy unchanged and, although global spin-rotations can cause such transformations, we want to avoid them by construction in the $\boldsymbol{\kappa}$ representation. We can therefore focus on only the OV or VO blocks of the two transformation matrices, leading to the relationship

$$\boldsymbol{U}\sin(\boldsymbol{\Sigma})\boldsymbol{V}^\intercal = \sin\frac{\theta}{2}(\boldsymbol{S}^{\mathrm{VO}}_{\alpha\beta} - \boldsymbol{S}^{\mathrm{VO}}_{\beta\alpha}). \tag{B13}$$

Since $\boldsymbol{\Sigma}$ is a diagonal matrix, one possible solution for the corresponding $\boldsymbol{\kappa}$ matrix is

$$\boldsymbol{\kappa} = \frac{\theta}{2}(\boldsymbol{S}^{\mathrm{VO}}_{\alpha\beta} - \boldsymbol{S}^{\mathrm{VO}}_{\beta\alpha}). \tag{B14}$$

Although this $\boldsymbol{\kappa}$ matrix does not exactly lead to the global spin-rotation (due to differences in the OO and VV blocks), we can view it as the combination of a global spin-rotation and a series of occupied-occupied or virtual-virtual transformations; since both can leave the energy unchanged, the combined matrix successfully represents the effect of a global spin rotation.

It is possible for this form of the $\boldsymbol{\kappa}$ matrix associated with global spin rotations to contain only zero values i.e. when $\left(\boldsymbol{S}^{\mathrm{VO}}_{\alpha\beta} - \boldsymbol{S}^{\mathrm{VO}}_{\beta\alpha}\right) = \mathbf{0}_{\mathrm{VO}}$. For example, $\boldsymbol{\kappa}$ is zero for a set of orbital coefficients satisfying the RHF constraint since the α orbitals are the same as the β orbitals, and thus the occupied α spatial orbitals must be strictly orthogonal to the virtual β spatial orbitals and *vice versa*. In this case, a global spin rotation leads to pure occupied-occupied and virtual-virtual transformations that are already excluded by the $\boldsymbol{\kappa}$ representation. More generally, a zero Hessian eigenvalue associated with a global spin rotation will only occur if the coefficients are not symmetric with respect to y-axis spin rotations, for example a spin-symmetry broken UHF solution. These zero eigenvalues are referred to as improper modes of the Hessian and are associated with breaking continuous spin symmetries.[116]

Appendix C: Distinguishing GHF Continuum Solutions

GHF solutions with $\langle \mathcal{S}^2 \rangle \neq 0$ form a one-dimensional continuum of stationary points in the direction of the corresponding zero Hessian eigenvector (Appendix B). Since there are an infinite number of possible stationary coefficients associated with each continuum, we consider two sets of coefficients that lie on the same continuum as equivalent. To identify whether two sets of coefficients ${}^x\boldsymbol{C}$ and ${}^w\boldsymbol{C}$ lie on the same GHF continuum, we must first establish a primary axis defined by the spin vector of each solution. Using the collinearity test introduced by Small *et al.*,[120] we define this primary axis as the

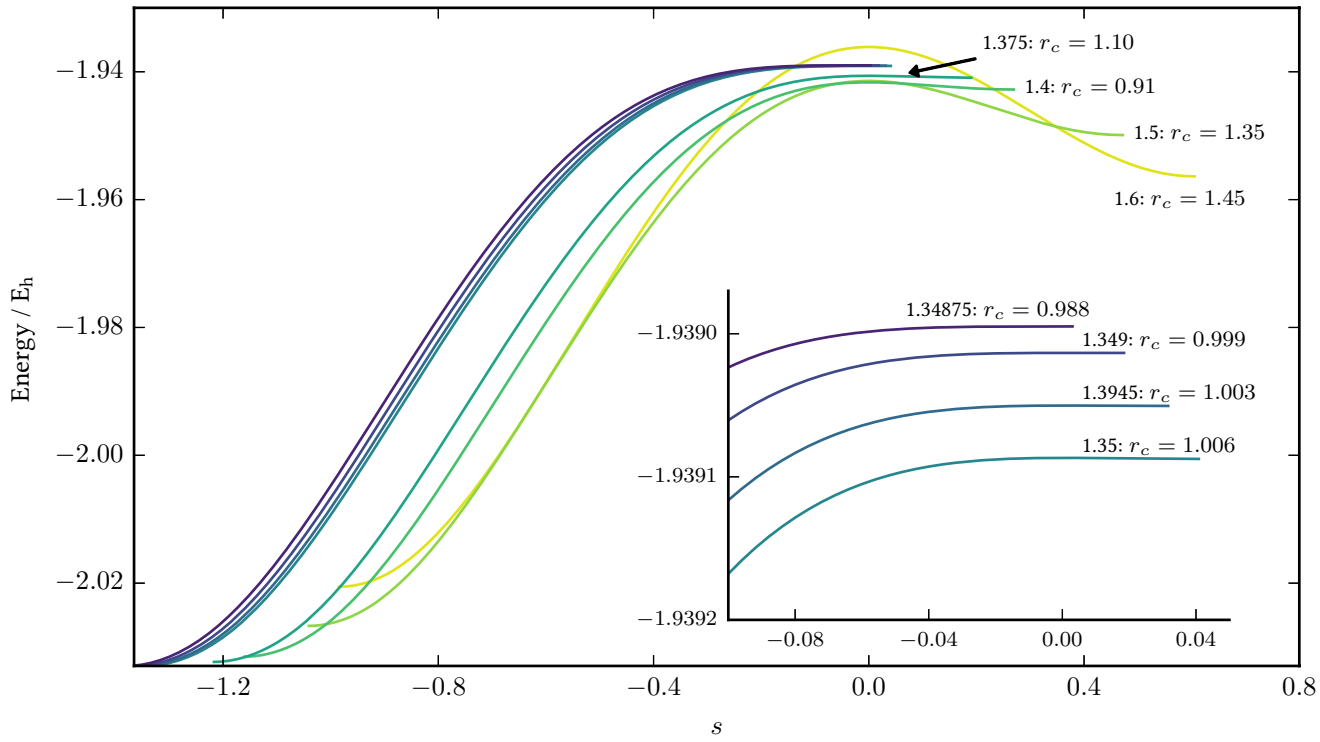

FIG. 12: Energy along selected pathways in square H_4 (3-21G) with side lengths as marked on the plot. The integrated path length, s, is the sum of the step magnitudes for the $\boldsymbol{\kappa}$ matrix variables (dimensionless). $r_c = 8\Delta V/|\lambda|(\Delta s)^2$ is the cusp ratio[46,118,119] calculated using the magnitude of the negative Hessian eigenvalue, λ, at the transition state. Here ΔV is the potential energy difference between the transition state and minimum, and Δs is the integrated path length. The ratio can also be calculated as $r_c = 4\Delta V/\lambda_{\min}(\Delta s)^2$ using the smallest Hessian eigenvalue, $\lambda_{\min}$, at the corresponding minimum, which gives the same trend. The magnified inset panel shows the results for the smaller side lengths from 1.3485 Å to 1.35 Å; the corresponding r_c values are unity within the limits of numerical precision for calculation of the steepest-descent pathways.

eigenvector of the A matrix with the lowest eigenvalue [see Eq. (11) in Ref 120]. In the case of a spin-collinear solution, this axis aligns with the spin-vector and the corresponding eigenvalue is zero.

Having identified the primary axis for each solution, we apply a global spin rotation to align this primary axis with the z-direction using Eq. (B4). We can then compare the two sets of coefficients using the wave function and density distance metrics defined in Eq. (12). For collinear solutions, it is possible for the primary spin axis identified from the collinearity test to be aligned parallel or antiparallel with the overall spin vector, i.e. with a positive or negative m_s value. However, once the primary axes of the two solutions are aligned, the two cases can be identified by applying a π spin-rotation to one set of coefficients, and the smaller of the two distances is then chosen.

Appendix D: Analysis of Cusp Catastrophe

The disappearance of the four-fold degenerate minima along the H_4 square stretch (Section III C) occurs at cusp catastrophes where one minimum coalesces with two index-1 saddle points to leave a single index-1 saddle point. To visualise this process, the steepest-descent pathways from one of these transition states are plotted at different bond lengths in Figure 12. The corresponding pathways were calculated using a second order method[71] implemented in the OPTIM program, with analytic second derivatives. The path length to the higher energy minimum decreases to 0.303×10^{-2} for the closest approach to the catastrophe, at a side length of 1.34875 Å. In this limit there is no significant difference between using the integrated path length and the straight line displacement between the stationary points in calculating the cusp ratio.[46,118] The displacements from the transition state parallel and antiparallel to the eigenvector corresponding to the unique negative Hessian eigenvalue were obtained using a golden section search with a maximum value of 0.004 Å. For a side length of 1.34875 Å the negative eigenvalue at the transition state is $-0.19345 \times 10^{-4}\,E_h/Å^2$, and the smallest eigenvalue at the relevant minimum is $0.96156 \times 10^{-5}\,E_h/Å^2$. The ratio of -2.01 is therefore close to the ideal value of -2, definitively identifying the presence of a cusp catastrophe.[46,118]

SUPPORTING INFORMATION

Orbital rearrangements for the UHF energy landscapes with $m_s = 1$ and 2.

REFERENCES

[1] Davidson, E. R.; Borden, W. T. Symmetry Breaking in Polyatomic Molecules: Real and Artifactual. *J. Phys. Chem.* **1983**, *87*, 4783.

[2] Fukutome, H. Unrestricted Hartree–Fock Theory and Its Applications to Molecules and Chemical Reactions. *Int. J. Quantum Chem.* **1981**, *20*, 955.

[3] Li, X.; Paldus, J. Do independent-particle=model broken-symmetry solutions contain more physics than the symmetry-adapted ones? The case of homonuclear diatomics. *J. Chem. Phys.* **2009**, *130*, 084110.

[4] Huynh, B. C.; Thom, A. J. W. Symmetry in Multiple Self-Consistent-Field Solutions of Transition-Metal Complexes. *J. Chem. Theory Comput.* **2020**, *16*, 904.

[5] Xie, Y.; Allen, W. D.; Yamaguchi, Y.; Schaefer, H. F. Is the oxywater radical cation more stable than neutral oxywater. *J. Chem. Phys.* **1996**, *104*, 7615.

[6] Barnes, L. A.; Lindh, R. Symmetry breaking in O_4^+: an application of the Brueckner coupled-cluster method. *Chem. Phys. Lett.* **1994**, *223*, 207.

[7] Auer, A. A.; Gauss, J. Orbital instabilities and spin-symmetry breaking in coupled-cluster calculations of indirect spin-spin coupling constants. *Chem. Phys.* **2009**, *356*, 7.

[8] Gilbert, A. T. B.; Besley, N. A.; Gill, P. M. W. Self-Consistent Field Calculations of Excited States Using the Maximum Overlap Method (MOM). *J. Phys. Chem. A* **2008**, *112*, 13164.

[9] Besley, N. A.; Gilbert, A. T. B.; Gill, P. M. W. Self-consistent-field calculations of core excited states. *J. Chem. Phys.* **2009**, *130*, 124308.

[10] Barca, G. M. J.; Gilbert, A. T. B.; Gill, P. M. W. Communication: Hartree–Fock description of excited states of H_2. *J. Chem. Phys.* **2014**, *141*, 111104.

[11] Barca, G. M. J.; Gilbert, A. T. B.; Gill, P. M. W. Simple Models for Difficult Electronic Excitations. *J. Chem. Theory Comput.* **2018**, *14*, 1501.

[12] Hait, D.; Head-Gordon, M. Excited State Orbital Optimization via Minimizing the Square of the Gradient: General Approach and Application to Singly and Doubly Excited States via Density Functional Theory. *J. Chem. Theory Comput.* **2020**, *16*, 1699.

[13] Carter-Fenk, K.; Herbert, J. State-Targeted Energy Projection: A Simple and Robust Approach to Orbital Relaxation of Non-Aufbau Self-Consistent Field Solutions. *J. Chem. Theory Comput.* **2020**, *XX*, XXXX.

[14] Jackels, C. F.; Davidson, E. R. The two lowest energy $^2A'$ states of NO_2. *J. Chem. Phys.* **1976**, *64*, 2908.

[15] Ayala, P. Y.; Schlegel, H. B. A nonorthogonal CI treatment of symmetry breaking in sigma formyloxyl radical. *J. Chem. Phys.* **1998**, *108*, 7560.

[16] Thom, A. J. W.; Head-Gordon, M. Hartree–Fock solutions as a quasidiabatic basis for nonorthogonal configuration interaction. *J. Chem. Phys.* **2009**, *131*, 124113.

[17] Burton, H. G. A.; Thom, A. J. W. General Approach for Multireference Ground and Excited States using Nonorthogonal Configuration Interaction. *J. Chem. Theory Comput.* **2019**, *15*, 4851.

[18] Mayhall, N. J.; Horn, P. R.; Sundstrom, E. J.; Head-Gordon, M. Spin-flip nonorthogonal configuration interaction: A variational and almost black-box method for describing strongly correlated molecules. *Phys. Chem. Chem. Phys.* **2014**, *16*, 22694.

[19] Jensen, K. T.; Benson, R. L.; Cardamone, S.; Thom, A. J. W. Modeling Electron Transfers Using Quasidiabatic Hartree–Fock States. *J. Chem. Theory Comput.* **2018**, *14*, 4629.

[20] Stuber, J. L.; Paldus, J. In *Fundamental World of Quantum Chemistry: A Tribute Volume to the Memory of Per-Olov Löwdin*; Brändas, E. K., Kryachko, E. S., Eds.; Kluwer Academic Publishers: Dordrecht, The Netherlands, 2003; Vol. 1; Chapter Symmetry Breaking in the Independent Particle Model, p 67.

[21] Lykos, P.; Pratt, G. W. Discussion on The Hartree–Fock Approximation. *Rev. Mod. Phys.* **1963**, *35*, 496.

[22] Löwdin, P.-O. Quantum Theory of Many-Particle Systems. III. Extension of the Hartree-Fock Scheme to Include Degenerate Systems and Correlation Effects. *Phys. Rev.* **1955**, *97*, 1509.

[23] Smeyers, Y. G.; Doreste-Suarez, L. Half-Projected and Projected Hartree–Fock Calculations for Singlet Ground States. I. Four-Electron Atomic Systems. *Int. J. Quantum Chem.* **1973**, *7*, 687.

[24] Jiménez-Hoyos, C. A.; Henderson, T. M.; Tsuchimochi, T.; Scuseria, G. E. Projected Hartree–Fock Theory. *J. Chem. Phys.* **2012**, *136*, 164109.

[25] Thom, A. J. W.; Head-Gordon, M. Locating Multiple Self-Consistent Field Solutions: An Approach Inspired by Metadynamics. *Phys. Rev. Lett.* **2008**, *101*, 193001.

[26] Tóth, Z.; Pulay, P. Finding symmetry breaking Hartree–Fock solutions: The case of triplet instability. *J. Chem. Phys.* **2016**, *145*, 164102.

[27] Thompson, L. M. Global elucidation of broken symmetry solutions to the independent particle model through a Lie algebraic approach. *J. Chem. Phys.* **2018**, *149*, 194106.

[28] Kowalski, K.; Jankowski, K. Towards Complete Solutions to Systems of Nonlinear Equations in Many-Electron Theories. *Phys. Rev. Lett.* **1998**, *81*, 1195.

[29] Čížek, J.; Paldus, J. Stability Conditions for the Solutions of the Hartree–Fock Equations for Atomic and Molecular Systems. Application to the Pi-Elecrton Model of Cyclic Polyenes. *J. Chem. Phys.* **1967**, *47*, 3976.

[30] Paldus, J.; Čížek, J. Stability Conditions for the Solutions of the Hartree–Fock Equations for the Simple Open-Shell Case. *Chem. Phys. Lett.* **1969**, *3*, 1.

[31] Seeger, R.; Pople, J. A. Self-consistent molecular orbital methods. XVIII. Constraints and stability in Hartree–Fock theory. *J. Chem. Phys.* **1977**, *66*, 3045.

[32] Roothaan, C. C. J. New Developments in Molecular Orbital Theory. *Rev. Mod. Phys.* **1951**, *23*, 69.

[33] Hall, G. G. The molecular orbital theory of chemical valency VIII. A method of calculation ionization. *Proc. Royal Soc. A* **1951**, *205*, 541.

[34] Van Voorhis, T.; Head-Gordon, M. A geometric approach to direct minimization. *Mol. Phys.* **2002**, *100*, 1713.

[35] Douady, J.; Ellinger, Y.; Subra, R.; Levy, B. Exponential transformation of molecular orbitals: A quadratically convergent SCF procedure. I. General formulation and application to closed-shell ground states. *J. Chem. Phys.* **1980**, *72*, 1452.

[36] Head-Gordon, M.; Pople, J. A. Optimization of Wave Function and Geometry in the Finite Basis Hartree–Fock Method. *J. Phys. Chem.* **1988**, *92*, 3063.

[37] Backsay, G. B. A quadratically convergent Hartree–Fock (QC-SCF) method. Application to open shell orbital optimization and coupled perturbed Hartree–Fock calculations. *Chem. Phys.* **1982**, *65*, 383.

[38] Sano, T.; l'Haya, Y. J. Constrained Newton approach to SCF calculations. *J. Chem. Phys.* **1991**, *95*, 6607.

[39] Thouless, D. J. Stability Conditions and Nuclear Rotations in the Hartree–Fock Theory. *Nucl. Phys.* **1960**, *21*, 225.

[40] Goings, J. J.; Ding, F.; Frisch, M. J.; Li, X. Stability of the complex generalized Hartree–Fock equations. *J. Chem. Phys.* **2015**, *142*, 154109.

[41] Burton, H. G. A.; Gross, M.; Thom, A. J. W. Holomorphic Hartree–Fock Theory: The Nature of Two-Electron Problems. *J. Chem. Theory Comput.* **2018**, *14*, 607.

[42] Igawa, A.; Fukutome, H. A New Direct Minimization Algorism for Hartree–Fock Calculation. *Prog. Theor. Phys.* **1975**, *54*, 1266.

[43] Stillinger, F. H.; Weber, T. A. packing structures and transitions in liquids and solids. *Science* **1984**, *225*, 983.

[44] Doye, J. P. K.; Wales, D. J. Saddle points and dynamics of Lennard-Jones clusters, solids, and supercooled liquids. *J. Chem. Phys.* **2002**, *116*, 3777–3788.

[45] Murrell, J. N.; Laidler, K. J. Symmetries of activated complexes. *Trans. Faraday. Soc.* **1968**, *64*, 371–377.

[46] Wales, D. J. *Energy Landscapes*; Cambridge University Press: Cambridge, 2003.

[47] Munro, L. J.; Wales, D. J. Defect migration in crystalline silicon. *Phys. Rev. B* **1999**, *59*, 3969–3980.

[48] Henkelman, G.; Jónsson, H. A dimer method for finding saddle points on high dimensional potential surfaces using only first derivatives. *J. Chem. Phys.* **1999**, *111*, 7010–7022.

[49] Kumeda, Y.; Munro, L. J.; Wales, D. J. Transition States and Rearrangement Mechanisms from Hybrid Eigenvector-Following and Density Functional Theory. Application to $C_{10}H_{10}$ and Defect Migration in Crystalline Silicon. *Chem. Phys. Lett.* **2001**, *341*, 185–194.

[50]Zeng, Y.; Xiao, P.; Henkelman, G. Unification of algorithms for minimum mode optimization. *J. Chem. Phys.* **2014**, *140*, 044115.

[51]Shao, Y. et al. Advances in molecular quantum chemistry contained in the Q-Chem 4 program package. *Mol. Phys.* **2015**, *113*, 184.

[52]OPTIM: A program for geometry optimisation and pathway calculations. http://www-wales.ch.cam.ac.uk/software.html.

[53]PATHSAMPLE: A program for generating connected stationary point databases and extracting global kinetics. http://www-wales.ch.cam.ac.uk/software.html.

[54]Head-Gordon, M.; Maslen, P. E.; White, C. A. A tensor formulation of many-electron theory in a nonorthogonal single-particle basis. *J. Chem. Phys.* **1998**, *108*, 616.

[55]Szabo, A.; Ostlund, N. S. *Modern Quantum Chemistry*; Dover Publications Inc., 1989.

[56]Edelman, A.; Tomás, A. A.; Smith, S. T. The geometry of algorithms with orthogonality constraints. *SIAM J. Sci. Comput.* **1998**, *20*, 303.

[57]Hammes-Schiffer, S.; Anderson, H. C. The advantages of the general Hartree–Fock method for future computer simulation of materials. *J. Chem. Phys.* **1993**, *99*, 1901.

[58]Slater, J. C. Magnetic Effects and the Hartree–Fock Equation. *Phys. Rev.* **1951**, *82*, 538.

[59]Pople, J. A. Electronic States and Wave Functions Associated with Orbital Energy Crossing. *Int. J. Quantum Chem.* **1971**, *5*, 172.

[60]Small, D. W.; Sundstrom, E. J.; Head-Gordon, M. Restricted Hartree Fock using complex-valued orbitals: A long-known but neglected tool in electronic structure theory. *J. Chem. Phys.* **2015**, *142*, 024104.

[61]Wales, D. J. Energy Landscapes: Some New Horizons. *Curr. Opin. Struct. Biol.* **2010**, *20*, 3–10.

[62]Joseph, J. A.; Röder, K.; Chakraborty, D.; Mantell, R. G.; Wales, D. J. Exploring biomolecular energy landscapes. *Chem. Commun.* **2017**, *53*, 6974–6988.

[63]Wales, D. J. Exploring Energy Landscapes. *Ann. Rev. Phys. Chem.* **2018**, *69*, 401–425.

[64]Nocedal, J. Updating quasi-Newton matrices with limited storage. *Mathematics of Computation* **1980**, *35*, 773–782.

[65]Broyden, C. G. The Convergence of a Class of Double-rank Minimization Algorithms 1. General Considerations. *J. Inst. Math. Appl.* **1970**, *6*, 76–90.

[66]Fletcher, R. A new approach to variable metric algorithms. *Comput. J.* **1970**, *13*, 317–322.

[67]Goldfarb, D. A family of variable-metric methods derived by variational means. *Math. Comput.* **1970**, *24*, 23–26.

[68]Shanno, D. F. Conditioning of quasi-Newton methods for function minimization. *Math. Comput.* **1970**, *24*, 647–656.

[69]Uppenbrink, J.; Wales, D. J. When do gradient optimizations converge to saddle- points? *Chem. Phys. Lett.* **1992**, *190*, 447–452.

[70]Wales, D. J.; Doye, J. P. K. Stationary points and dynamics in high-dimensional systems. *J. Chem. Phys.* **2003**, *119*, 12409–12416.

[71]Page, M.; McIver, J. W. ? *J. Chem. Phys.* **1988**, *88*, 922.

[72]Becker, O. M.; Karplus, M. The topology of multidimensional potential energy surfaces: Theory and application to peptide structure and kinetics. *J. Chem. Phys.* **1997**, *106*, 1495–1517.

[73]Wales, D. J.; Miller, M. A.; Walsh, T. R. Archetypal energy landscapes. *Nature* **1998**, *394*, 758–760.

[74]Burton, H. G. A.; Thom, A. J. W. Holomorphic Hartree–Fock Theory: An Inherently Multireference Approach. *J. Chem. Theory Comput.* **2016**, *12*, 167.

[75]Mori-Sánchez, P.; Cohen, A. J. Qualitative breakdown of the unrestricted Hartree–Fock energy. *J. Chem. Phys.* **2014**, *141*, 164124.

[76]Jankowski, K.; Paldus, J. Applicability of Coupled-Pair Theories to Quasi-degenerate Electronic States: A Model Study. *Int. J. Quantum Chem.* **1980**, *18*, 1243.

[77]Bulik, I. W.; Henderson, T. M.; Scuseria, G. E. Can Single-Reference Coupled Cluster Theory Describe Static Correlation? *J. Chem. Theory Comput.* **2015**, *11*, 3171.

[78]Van Voorhis, T.; Head-Gordon, M. Benchmark variational coupled cluster doubles results. *J. Chem. Phys.* **2000**, *113*, 8873.

[79]Blinkley, J. S.; Pople, J. A.; Hehre, W. J. Self-Consistent Molecular Orbital Methods. 21. Small Split-Valence Basis Sets for First-Row Elements. *J. Am. Chem. Soc.* **1980**, *102*, 939.

[80]Leone, R. E.; v. R. Schleyer, P. *Angew. Chem. Int. Ed. Engl.* **1970**, *9*, 860.

[81]Wales, D. J.; Doye, J. P. K.; Miller, M. A.; Mortenson, P. N.; Walsh, T. R. Energy landscapes: from clusters to biomolecules. *Adv. Chem. Phys.* **2000**, *115*, 1–111.

[82]Nourse, J. G. *J. Am. Chem. Soc.* **1980**, *102*, 4883.

[83]Keutsch, F. N.; Saykally, R. J.; Wales, D. J. Bifurcation tunneling dynamics in the water trimer. *J. Chem. Phys.* **2002**, *117*, 8823–8835.

[84]Cole, W. T. S.; Farrell, J. D.; Wales, D. J.; Saykally, R. J. Structure and torsional dynamics of the water octamer from THz laser spectroscopy near 215 μm. *Science* **2016**, *352*, 1194–1197.

[85]Richardson, J. O.; Pérez, C.; Lobsiger, S.; Reid, A. A.; Temelso, B.; Shields, G. C.; Kisiel, Z.; Wales, D. J.; Pate, B. H.; Althorpe, S. C. Concerted hydrogen-bond breaking by quantum tunneling in the water hexamer prism. *Science* **2016**, *351*, 1310–1313.

[86]Fukui, K. a formulation of the reaction coordinate. *J. Phys. Chem.* **1970**, *74*, 4161.

[87]Pearson, R. G. symmetry rules for chemical reactions. *Acc. Chem. Res.* **1971**, *4*, 152.

[88]McIver, J. W.; Komornicki, A. *Chem. Phys. Lett.* **1971**, *10*, 303.

[89]Metiu, H.; Ross, J.; Silbey, R.; George, T. F. *J. Chem. Phys.* **1974**, *61*, 3200.

[90]Pechukas, P. on simple saddle points of a potential surface, the conservation of nuclear symmetry along paths of steepest descent, and the symmetry of transition states. *J. Chem. Phys.* **1976**, *64*, 1516.

[91]Kohn, W.; Sham, L. J. Self-Consistent Equations Including Exchange and Correlation Effects. *Phys. Rev.* **1965**, *140*, A1133.

[92]Perdew, J. P.; Savin, A.; Burke, K. Escaping the symmetry dilemma through a pair-density interpretation of spin-density functional theory. *Phys. Rev. A* **1995**, *51*, 4531.

[93]Kendall, R. A.; Dunning, T. H.; Harrison, R. J. Electron affinities of the first-row atoms revisisted. Systematic basis sets and wave functions. *J. Chem. Phys.* **1992**, *96*, 6796.

[94]Becke, A. D. A new mixing of Hartree–Fock and local density-functional theories. *J. Chem. Phys.* **1993**, *98*, 1372.

[95]Stephens, P. J.; Devlin, F. J.; Chabalowski, C. F.; Frisch, M. J. Ab Inition Calculation of Vibrational Absorption and Circular Dichoism Spectra using Density Functional Force Fields. *J. Phys. Chem.* **1994**, *98*, 11623.

[96]Coulson, C. A.; Fischer, I. XXXIV. Notes on the molecular orbital treatment of the hydrogen molecule. *Philos. Mag.* **1949**, *40*, 386.

[97]Zarotiadis, R. A.; Burton, H. G. A.; Thom, A. J. W. Towards a Holomorphic Density-Functional Theory. **2020**, arXiv:2008.02586.

[98]Stanton, R. E. Multiple Solutions to the Hartree–Fock Problem. I. General Treatment of Two-Electron Closed-Shell Systems. *J. Chem. Phys.* **1968**, *48*, 257.

[99]Fukutome, H. Theory of the Unrestricted Hartree–Fock Equation and Its Solutions. IV: Behaviour of UHF Solutions in the Vicinity of Interconnecting Instability Threshold. *Prog. Theor. Phys.* **1975**, *53*, 1320.

[100]Mestechkin, M. Potential energy surface near the Hartree–Fock Instability Threshold. *J. Mol. Struct.: THEOCHEM* **1988**, *181*, 231.

[101]Hiscock, H. G.; Thom, A. J. W. Holomorphic Hartree–Fock Theory and Configuration Interaction. *J. Chem. Theory Comput.* **2014**, *10*, 4795.

[102]Casanova, D.; Krylov, A. I. Spin-flip methods in quantum chemistry. *Phys. Chem. Chem. Phys.* **2020**, *22*, 4326.

[103]Limacher, P. A.; Kim, T. D.; Ayers, P. W.; Johnson, P. A.; De Baerdemacker, S.; Van Neck, D.; Bultinck, P. The influence of orbital rotation on the energy of closed-shell wavefunctions. *Mol. Phys.* **2014**, *112*, 853.

[104]Jiménez-Hoyos, C. A.; Henderson, T. M.; Scuseria, G. E. Generalized Hartree–Fock Description of Molecular Dissociation. *J. Chem. Theory Comput.* **2011**, *7*, 2667.

[105]Li, Z.; Scheraga, H. A. Monte Carlo-minimization approach to the multiple-minima problem in protein folding. *Proc. Natl. Acad. Sci. USA* **1987**, *84*, 6611–6615.

[106]Wales, D. J.; Doye, J. P. K. Global optimization by basin-hopping and the lowest energy structures of Lennard-Jones clusters containing up to 110 atoms. *J. Phys. Chem. A* **1997**, *101*, 5111–5116.

[107]Wales, D. J.; Scheraga, H. A. Global optimization of clusters, crystals and biomolecules. *Science* **1999**, *285*, 1368–1372.

[108]Dong, X.; Mahler, A. D.; Kempfer-Robertson, E. M.; Thompson, L. M. Global Elucidation of Self-Consistent Field Solution Space Using Basin Hopping. *J. Chem. Theory Comput.* **2020**, *16*, 5635.

[109]Ye, H.-Z.; Welborn, M.; Ricke, N. D.; Van Voorhis, T. σ-SCF: A direct energy-targeting method to mean-field excited states. *J. Chem. Phys.* **2017**, *147*, 214104.
[110]Doye, J. P. K.; Wales, D. J. Comment on "Quasisaddles as relevant points of the potential energy surface in the dynamics of supercooled liquids" [J. Chem. Phys. 116, 10297 (2002)]. *J. Chem. Phys.* **2003**, *118*, 5263–5264.
[111]Ye, H.-Z.; Van Voorhis, T. Half-Projected σ Self-Consistent Field for Electronic Excited States. *J. Chem. Theory Comput.* **2019**, *15*, 2954.
[112]Fukutome, H. Theory of the Unrestricted Hartree–Fock Equation and Its Solutions. I. *Int. J. Quantum Chem.* **1971**, *45*, 1382.
[113]Weinberg, S. *The Quantum Theory of Fields*; Cambridge University Press: Cambridge, 1995; Vol. 1.
[114]Burton, H. G. A.; Thom, A. J. W.; Loos, P.-F. Parity-Time Symmetry in Hartree–Fock Theory. *J. Chem. Theory Comput.* **2019**, *15*, 4374.
[115]Smeyers, Y. G.; Delgado-Barrio, G. Half-Projected and Projected Hartree–Fock Calculations for Singlet Ground States. II. Lithium Hydride. *Int. J. Quantum Chem.* **1974**, *8*, 733.
[116]Cui, Y.; Bulik, I. W.; Jiménez-Hoyos, C. A.; Henderson, T. M.; Scuseria, G. E. Proper and improper zero energy modes in Hartree–Fock theory and their relevance for symmetry breaking and restoration. *J. Chem. Phys.* **2013**, *139*, 154107.
[117]Hutter, J.; Parrinello, M.; Vogel, S. Exponential transformation of molecular orbitals. *J. Chem. Phys.* **1994**, *101*, 3862.
[118]Wales, D. J. A Microscopic Basis for the Global Appearance of Energy Landscapes. *Science* **2001**, *293*, 2067–2069.
[119]Bogdan, T. V.; Wales, D. J. New results for phase transitions from catastrophe theory. *J. Chem. Phys.* **2004**, *120*, 11090–11099.
[120]Small, D. W.; Sundstrom, E. J.; Head-Gordon, M. A simple way to test for collinearity in spin symmetry broken wave functions: General theory and application to generalized Hartree Fock. *J. Chem. Phys.* **2015**, *142*, 094112.